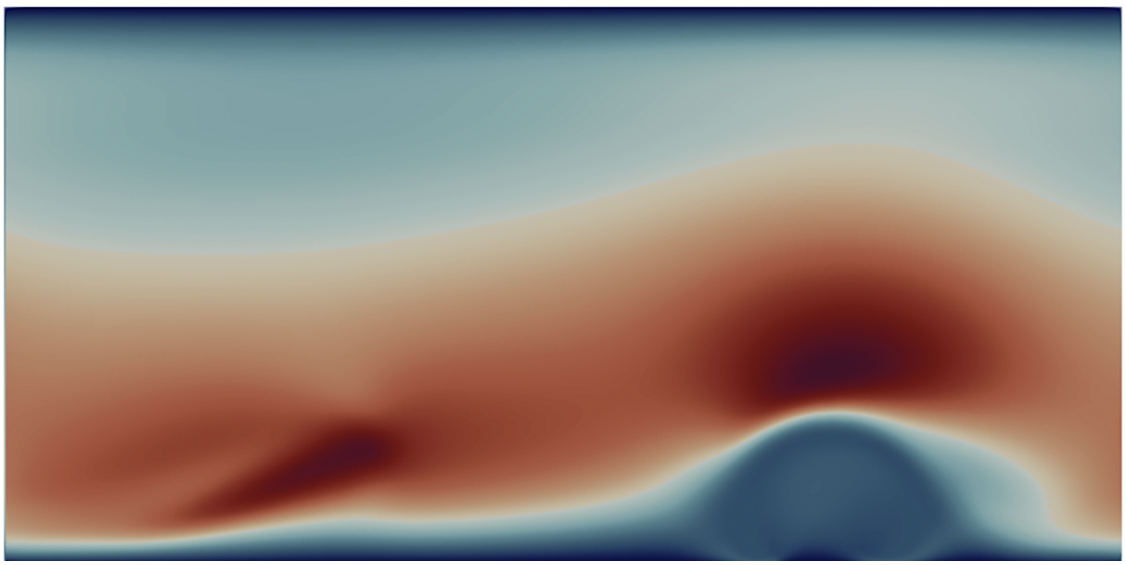

Numerical simulation of wetting on vehicles' windshields

Master's thesis in Master of automotive Engineering

ARMITA KARIMI

DEPARTMENT OF MECHANICS AND MARITIME SCIENCE

CHALMERS UNIVERSITY OF TECHNOLOGY
Gothenburg, Sweden 2022
www.chalmers.se

Master's thesis 2022

Numerical simulation of wetting on vehicles' windshields

ARMITA KARIMI

CHALMERS
UNIVERSITY OF TECHNOLOGY

Department of Mechanics and Maritime Science
Fluid Division
Name of research group (if applicable)
Chalmers University of Technology
Gothenburg, Sweden 2022

Numerical simulation of wetting and icing on vehicle's windshield

ARMITA KARIMI

Supervisor: Luca Brandt, KTH Royal Institute of Technology
Examiner: Gaetano Sardina, Chalmers University of Technology

Master's Thesis 2022
Department of Mechanics and Maritime Science
Fluid Division

Chalmers University of Technology
SE-412 96 Gothenburg
Telephone +46 31 772 1000

Typeset in LaTeX
Printed by Chalmers Reproservice
Gothenburg, Sweden 2022

Numerical simulation of wetting and icing on vehicle's windshield

ARMITA KARIMI
Department of Mechanics and Maritime Science
Chalmers University of Technology

Abstract

In this project, the spreading dynamics of a single droplet over surfaces with different wettability conditions are studied by means of a series of numerical simulations aiming to model the motion of a rain droplet over vehicles' windshields. To do so, a Cahn-Hilliard formulation of the Phase Field (PF) is employed.

The wettability of the surface is modelled by imposing a contact angle. During the spreading process, the three-phase contact line moves over the surface while the prescribed contact angle is fulfilled. to successfully remove the well-known contact line singularity problem, a dynamic contact angle together with a slip velocity boundary conditions are imposed at the surface.

Given the variety of parameters governing the dynamics of the problem, including properties of each phase (viscosity, density, etc.) the angle of the windshields, surface wettability, relative wind velocity, thermo-physical properties (such as ambient temperature ,cabin temperature) and considering computational costs, the focus of this study is on the effects of windshields' angle, relative wind velocity and surface wettability. To further investigate the problem, several additional simulations have been performed for selected cases to scrutinize the effects of fluid properties.

Keywords:Phase Field Method(PFM), Contact line dynamic, Interface, Diffuse Interface(DI) methods

Acknowledgements

First, I want to thank my supervisor Prof. Luca Brandt at KTH royal Institute of Technology for giving me the opportunity to conduct this master's thesis. I have learned so much more than I thought was possible and it has motivated me to continue learning even more within the field of fluid mechanics.

I would like to express my gratitude to my co-supervisor Armin Shahmardi for always being supportive with everyday issues and put a lot of extra effort and time supporting me with discussions, finalization of the report and preparation of the presentation.

Finally, thanks to my examiner, Assoc. Prof. Gaetano Sardina, and to all professors at Chalmers University of Technology for all knowledge and skills that I have gained during my master program at Chalmers.

Armita Karimi, Gothenburg,August 2022

List of Acronyms

Below is the list of acronyms that have been used throughout this thesis listed in alphabetical order:

PFM	Phase Field Method
DI	Diffuse Interface
VOF	Volume Of Fluid
IBM	Immersed Boundary Method

Nomenclature

Below is the nomenclature of symbols along their definitions that have been used throughout this thesis.

Symbols

C	Concentration
Ca	Capillary number
Cn	Cahn number
f	Free energy per unit volume (J/m^3)
F	Body forces
l_s	Slip length (m)
P	Pressure
n_i	Normal vector
Re	Reynolds number
u_i	Face centred velocity vector (m/s)
u_s	Slip velocity (m/s)
α	Rotation angle of the surface (Degree)
Γ	Auxiliary variable for semi-implicit method. ($1/m^2$)
Δt	Time step (s)
θ	Contact angle (Degree)
ρ	Mass density (kg/m^3)
σ	Surface tension coefficient (N/m)
ϕ	Chemical potential per unit volume (J)

Contents

List of Figures

List of Tables

1

Introduction

1.1 Motivation

The motion of a three-phase contact line and wetting occurs in nature as well as in numerous industrial applications. Formation of dew on lotus leaves early in the morning and the motion of raindrops on windows are two ubiquitous examples of wetting in nature.

On the other hand, contact line dynamics and wettability of the surface play important role in many industries including any form of droplet spreading on a solid surface, coating flows and displacement flows, automotive industry, microelectronics cooling, nucleate boiling, etc . Therefore, understanding the underlined physics of contact line dynamics is crucial to optimise the performance of devices in the abovemention industries. In particular, in automotive industry, drivers' vision and the roads visibility are great importance under a wide range of environmental conditions. Hence, a self cleaning mechanism for the windshields resulting quick departure of the droplets which improves drivers' vision and reduces the possibility of ice formation (in cold countries such as Sweden) is desired.

During the last decades many researchers studied the droplet spreading by means of experiments, numerical simulations, and analytical approaches. However the well-known contact line singularity [1] limits the analytical studies whereas setup constraints make the experimental studies a cumbersome task[2]. On the other hand thanks to advancements in computational resources numerical simulation proved to be powerful tools for an in-depth study of the spreading problem.

In this project, a Phase-Field Model (hereafter will be referred to as PFM) is employed to simulate droplet spreading and properly imposing the three phase contact angle. The diffuse nature of the model together with dynamic contact angle and slip boundary conditions provide a reliable numerical framework to tackle the well-known contact line singularity. In particular, the Cahn-Hilliard [3] equation and the boundary conditions are derived based on the free energy of the system providing a thermodynamicaly consistent representation of the interface. The desired contact angle is imposed as a boundary condition to control the wettability of the surface. If the prescribed contact angle is obtuse the surface is called hydrophobic whereas an acute value of the contact angle models a hydrophilic surface.

1.2 Analytical solution

Despite the importance and numerous studies have been performed, the physics of moving contact lines is poorly understood and it is still a matter of debate. The difficulty in studying the contact line movement originates in the so-called "contact line singularity". This issue was first discussed by Moffat [4].

Here in this section, the approaches which helps to remove the singularities close to the moving contact line are mentioned. As the first solution, applying Navier boundary condition which is a slip velocity near contact line could be a solution [5]. Also, modelling the dynamic contact angle and the formation of a precursor film are the two other suggested solutions[6]. Moreover, Dervaux and Limat [7]used an exact Green function method to calculate analytically the substrate deformations near straight contact lines on a soft, linearly elastic incompressible solid, having a uniform surface tension . This generalized Flamant–Cerruti problem of a single contact line which is regularized by introducing a finite width for the contact line. Another study with an analytical expression is done by Yuri Yu. Tarasevich [8] of hydrodynamic potential inside an evaporating sessile drop with pinned contact line is found. The problem is considered for a hemispherical drop (with the contact angle of 90°) at the very early stages of the evaporation process when the shape of the drop is still a hemisphere and the evaporation field is uniform. The capillary flow carries a fluid from the drop apex to the contact line. Comparison with the published calculations performed using lubrication approximation (very thin drop) suggests that qualitative picture of the capillary flow is insensitive to the ratio of initial drop height to the drop radius.

1.3 Experiments

Many researchers studied contact line dynamics by performing experiments.] Salem, T.K. et al [9], Schäffer and Wong [10] in which a video microscopy is used to study the pinning dynamics of air/water contact lines in vertical glass capillaries. Furthermore,[11] suggest that the dynamic contact angle formed between the free surface of a liquid and a moving solid boundary at a fixed contact-line speed depends on the flow field and geometry near the moving contact line. Moreover,in some fields of technological application, for instance superhydrophobic materials, such as protection against corrosion, icing, and capillary condensation, or micro fluidics applications, a superhydrophobic surface has to operate in contact with aggressive aqueous media. Therefore, the peculiarities of behaviour of hydrophobic and superhydrophobic surfaces on prolonged contact with water and the mechanisms of possible degradation of superhydrophobicity need to be discussed. In Boinovich and Emelyanenko study [12], a consideration of the physicochemical processes accompanying the contact of hydrophobic and superhydrophobic materials with water, acid, alkaline and saline aqueous solutions is presented on the basis of experimental data on three-phase equilibrium obtained by the sessile drop method. Also,the basic

mechanisms of the liquid spreading on a rough surface and the entrapped gas under a drop had been discussed in Wang, J. et al [13]. Based on the mechanisms and experiment, hydrophobicity of the four lotus leaf surfaces was analyzed. The investigation results showed that the hydrophobicity of the front surfaces was dominated by the entrapped gas under the drop and the absolute stable position of the contact line while the back surfaces by metastable positions of the contact line, resulting in the ultrahydrophobicity on the front surfaces and large contact angle hysteresis on the back surfaces. There is also a study done by Mark Wilson an others [11] experimentally which suggest that the dynamic contact angle formed between the free surface of a liquid and a moving solid boundary at a fixed contact-line speed depends on the flow field and geometry near the moving contact line. Hence, examined quantitatively whether or not it is possible to attribute this effect to the bending of the free surface due to hydrodynamic stresses acting upon it and therefore interpret the results in terms of the so-called “apparent” contact angle.

1.4 Numerics

As an alternative approach for studying the moving contact line problem, different numerical methods have been proposed for tracking the interface and reconstructing the contact line. The interface tracking methods can be divided into two main categories, namely Eulerian and Lagrangian methods.

Starting from the latter, in Lagrangian approach the interface is initially marked by some Lagrangian grid points (markers) while the governing equations are discredited on another numerical mesh. By solving the governing equations on the numerical mesh and obtaining the velocity field, the location of the interface markers are updated based on the interpolated values of the velocity field on the Lagrangian points. Immersed Boundary Method (IBM) and Front tracking are examples of methods Lagrangian approach [14] . Note that in a Lagrangian approach there are two different sets of grid points and the algorithm requires continues interpolations of field variables between the two grid points. Here in this project the Phase Field Method (PFM) used which is an approach to model moving contact line.

On the other hand, in an Eulerian approach the interface is detected by transporting a continues color function. The value of the color function changes from one phase to another one (for instance -1 in one phase and +1 in another). Hence, the transport equation of the color function is discretized on the same grid point as the other equations [15]. Level-set, Volume of Fluid (VOF) [16], Diffuse Interface (DI) method, and in particular Phase Field Model (PFM) are examples of Eulerian approachs.
In many fields of research, in particular wetting studies and phase change phenomena, Eulerian interface tracking approaches proved to be more efficient for different reasons the most obvious one is less computational cost. Eulerian approaches can be divided into two main categories namely sharp interface methods and diffuse interface methods. In sharp interface methods the interface is assumed to have no

thickness and the fluid properties vary discontinuously over the interface. Hence, to tackle these discontinuities sharp interface methods require extra conditions to be satisfied at the interface (known as jump conditions). However, in diffuse interface methods, the interface is assumed to have a finite thickness much thicker than the real physical one. These property of the method provide continuous variation of the fluid properties across the interface and eliminates any extra jump conditions.

Diffuse interface models have also been used widely to study the contact line dynamics. The transport equation of the color function in DI methods is an advection-diffusion equation; this diffusive property of the interface culminates in removing the contact line singularity. Particularly, the well-known free energy based formulation of DI methods (PFM) has attracted lots of attentions in wetting and phase change studies .

Moreover, there are many research have been done with different conditions with numerical method such as Peter Spelt study [17] in which the predictive capability offered by the computational methods. Several challenges rather unique to this area need to be overcome, however, notably regarding the conditions near a moving contact line and the very large separation of length scales in these flows. The main models for moving contact lines summarized and follow with an overview of computational methods that includes direct continuum approaches and macroscale models that resolve only the large-scale flow by modeling the effects of the conditions near the contact line using theory. Results are presented for contact-line motion on ideal as well as patterned and grooved surfaces and for extensions to account for complexities such as thermocapillarity and phase change.

1.5 Project objective

The aim of this project is to study droplet spreading over inclined flat surfaces with different inclination angles and wettabilty conditions representing a rain droplet spreading over vehicles' windshields. To do so, a Cahn-Hilliard formulation of DI method together with dynamic contact angle and slip velocity boundary conditions are used. Effects of different values for inclination angle, contact angle and relative velocity of the wind on spreading radius and center of mass velocity have been studied. Moreover, to understand the role of different fluid properties several additional simulations have been performed for some selected cases.

1.6 Limitations

Considering the presence of many parameters affecting the dynamic of the droplet together with computational costs all the simulations performed in this thesis are constraint with the following assumptions.

- The simulation are limited to two dimensions in the space.

- Among different parameters, in this study, the role of contact angle and inclination angle are studied while all the other properties are affects except for selected cases.
- For simplicity in the simulation setup the relative velocity of the wind is modelled as a couette flow setup.
- The fourth order nature of Cahn-Hilliard equation requires the presence of several grid points within the interface. To fulfill this criteria, a fine numerical mesh is generated for this study resulting in expensive simulations. Thus, all the simulations have been run on supercomputers.
- The use of super computers available at KTH for the simulations resulted in a waiting times in the queue.

2

Theory

In this chapter, the mathematical formulation of the Cahn-Hilliard equation is represented in section 2.1. Next in section 2.2 the governing equation of the fluid flow (Navier-Stokes equation) is explained followed by section 2.3 where the proper boundary conditions for the contact angle and slip velocity are elaborated.

2.1 Cahn-Hilliard formulation

Phase Field Method (PFM) is a mathematical model for tracking the interface of two fluids.

The basic idea the of Phase Field Method originates in the pioneer work of Van der Waals where the free energy of a system of two immiscible fluids is represented as the summation of two main components, namely interfacial free energy and the bulk free energy as follows:

$$f = \frac{1}{2}\epsilon\sigma\frac{\partial C}{\partial x_i}\frac{\partial C}{\partial x_i} + \frac{\sigma}{\epsilon}\psi(C), \tag{2.1}$$

where C is the order parameter(also called color function or indicator function) which varies from -1 in one phase to +1 in the other to identify two different phases. $\psi = \frac{(c^2-1)^2}{4}$ is a double-well function which models the fluid components' immiscibility and has two minima corresponding to the two stable phases. σ and ϵ indicate the surface tension coefficient between the two and the interface thickness, respectively.

By definition, the chemical potential ϕ in a thermodynamic system can be obtain as the variation of the total free energy with respect to order parameter $\phi = \frac{F}{C}$:

$$\phi = \frac{\sigma}{\epsilon}\psi'(C) - \sigma\epsilon\frac{\partial}{\partial x_i}(\frac{\partial C}{\partial x_i}). \tag{2.2}$$

Any gradient of the chemical potential results in the diffusion of the interface which moves the interafce from the regions with higher chemical potential towards the regions with lower ones. Moreover, the interface of the two fluids can be convected with the fluid flow. Based on this idea Cahn and Hilliard formularted an advection-diffusion equation for the transport of the interface:

$$\frac{\partial C}{\partial t} + u_i \frac{\partial C}{\partial x_i} = \frac{3}{2\sqrt{2}} \frac{\partial}{\partial x_i}(M \frac{\partial \phi}{\partial x_i}), \tag{2.3}$$

where u_i represents the fluid flow velocity and M is the mobility coefficient which controles the diffusion strength.

2.2 Navier-Stokes equations

The dynamics of the fluid flow is modelled using Navier-Stokes equation:

$$\frac{\partial(\rho u_i)}{\partial t} + \frac{\partial}{\partial x_j}(\rho u_i u_j) = -\frac{\partial P}{\partial x_i} + \frac{\partial}{\partial x_j}(\mu(\frac{\partial u_i}{\partial x_j} + \frac{\partial u_j}{\partial x_i})) + \phi \frac{\partial C}{\partial x_i}, \tag{2.4}$$

where P is the pressure, μ is the dynamic viscosity, and ρ denotes the density. Note that the density and the viscosity of the fluid varies continuously from the ones of the first fluid to those of the second fluid as follows:

$$\rho(C) = \frac{(C+1)\rho_2 - (C-1)\rho_1}{2}, \mu(C) = \frac{(C+1)\mu_2 - (C-1)\mu_1}{2} \tag{2.5}$$

In equation 2.4, $\phi \frac{\partial C}{\partial x_i}$ represents the interfacial forces acting on the fluid elements at the interface. The system of two immicible fluid in this study is assumed to be incompressible. Thus the fluid flow is expected to be divergence free(continuity equation).

$$\frac{\partial u_i}{\partial x_i} = 0 \tag{2.6}$$

Where $\phi \frac{\partial C}{\partial x_i}$indicates the surface tension force at the interface and equation 2.6 represents mass conservation for incompressible fluids.

2.3 Boundary Conditions

Considering the third phase as a solid wall (in this study represents the vehicles' windshields), a third term must be added to free energy equation due to the contribution of the solid substrate to the total free energy of the system. This term (solid free energy) controls the wettability of the wall. In other words the larger the solid free energy the stronger the molecular interaction between the solid and fluid atoms resulting in a more hydrophilic surface. The complete free energy of the system in a presence of a slid wall is expressed as follows:

$$f = \int (\frac{1}{2}\epsilon\sigma \frac{\partial C}{\partial x_i}\frac{\partial C}{\partial x_i} + \frac{\sigma}{\epsilon}\psi(C))dV + \int (\sigma_{sg} + (\sigma_{sl} - \sigma_{sg}))g(c)d\Gamma, \tag{2.7}$$

where $\sigma_{sl}$and σ_{sg} are the surface tension coefficients between solid-liquid and solid-gas, and $d\Gamma$ is the solid area element.
According to Figure 2.1 ,the surface tension coefficient between any pair of phases can be related to the equilibrium contact angle θ_e through Young's equation[18]:

$$\cos(\theta_e)\sigma_{lg} = \sigma_{sg} - \sigma_{sl}. \tag{2.8}$$

By replacing the last term of equation 2.7 with equation 2.8 and minimising the total free energy of the system, the dynamic contact angle boundary conditions is obtained as follows [20]:

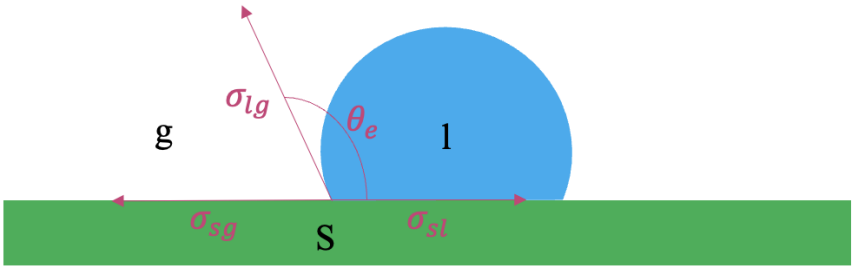

Figure 2.1: Sketch of contact angle

$$\mu_f \epsilon (\frac{\partial C}{\partial t} + u_i \frac{\partial C}{\partial x_i}) = \sigma \epsilon \frac{3}{2\sqrt{2}} \frac{\partial C}{\partial x_i} n_i + \sigma \cos(\theta_{eq}) g'(C) \tag{2.9}$$

Where n_i is the vector normal to the solid surface and μ_f and θ_{eq} are the contact line friction coefficient and the equilibrium contact angle respectively.
To avoid mass penetration at the wall a Neumann boundary condition for the chemical potential is imposed at the wall:

$$\frac{\partial \phi}{\partial x_i} n_i = 0 \tag{2.10}$$

Finally, in the case of non-zero wall slip velocity, the following equation can be solved together with the other boundary conditions to obtain the slip velocity at the wall [1]:

$$\frac{\mu}{l_s} u_{js} t_j = \mu \frac{\partial (u_j t_j)}{\partial (x_i n_i)} - [\frac{3}{2\sqrt{2}} \frac{\partial (C)}{\partial (x_i)} n_i + \sigma \cos(\theta_e q) g\prime(C)] \frac{\partial (C)}{\partial (x_j)} t_j \tag{2.11}$$

where l_s is the slip length and slip velocity defined as is represented in Figure 2.2

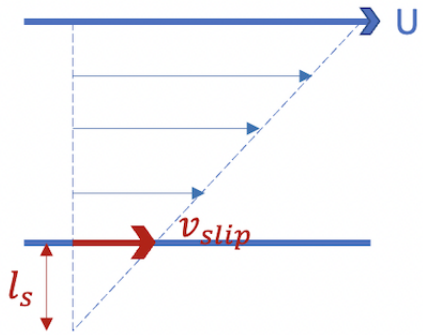

Figure 2.2: Sketch of slip length

3

Methods

Here in this section there are two subsection in which the numercal method and boundary condition are discussed distinctly. To begin with, the methods which used in general during this thesis project are mentioned as follows.

Diffuse interface models have been used extensively to study the contact line dynamics. Among different diffuse interface models, the phase-field method has become fairly popular. In the initial weeks of the project, most of the time is spent on understanding of the Phase Field method from the prescribed literature *A fully Eulerian hybrid immersed boundary-phase field model for contact line dynamics on complex geometries* [15] . This step in the project is critical since the Phase Field method is different to the other methods used and a thorough understanding of the method is required to interpret results and change parameters in the project work further on.

In all kind of diffuse interface models, an order parameter is defined in order to characterize different phases which is mentioned in theory section. The interface has a finite thickness in these methods which results in varying fluid properties smoothly but significantly from one phase to another one. This assumption allows tracking the interface by solving an advection-diffusion equation for the order parameter.

This is followed by getting familiarized with the ***Fortran*** code, ***MPI parallel processing*** and ***Paraview*** visualization tool, which are the project tools to be used for this analysis.

3.1 The full system of equation

The full system of equations which needed to be solved, introduced in the theory section and can be summarised as follows:

$$\frac{\partial(\rho u_i)}{\partial t} + \frac{\partial}{\partial x_j}(\rho u_i u_j) = -\frac{\partial P}{\partial x_i} + \frac{\partial}{\partial x_j}(\mu(\frac{\partial u_i}{\partial x_j} + \frac{\partial u_j}{\partial x_i})) + \phi\frac{\partial C}{\partial x_i} + F_b \tag{3.1}$$

$$\frac{\partial u_i}{\partial x_i} = 0 \tag{3.2}$$

$$\frac{\partial C}{\partial t} + u_i \frac{\partial C}{\partial x_i} = \frac{3}{2\sqrt{2}} \frac{\partial}{\partial x_i}(M \frac{\partial \phi}{\partial x_i}) \tag{3.3}$$

$$\phi = \frac{\sigma}{\epsilon}\psi'(C) - \sigma\epsilon \frac{\partial}{\partial x_i}(\frac{\partial C}{\partial x_i}) \tag{3.4}$$

Where F_b indicates the body forces (such as the gravitational force in this case).

The corresponding boundary conditions for the system of equations, reads as follows.

$$\mu_f \epsilon(\frac{\partial C}{\partial t} + u_i \frac{\partial C}{\partial x_i}) = \sigma\epsilon \frac{3}{2\sqrt{2}} \frac{\partial C}{\partial x_i} n_i + \sigma \cos(\theta_{eq}) g'(C) \tag{3.5}$$

$$\frac{\partial(\phi)}{\partial x_i} n_i = 0 \tag{3.6}$$

$$\frac{\mu}{l_s} u_{js} t_j = \mu \frac{\partial(u_j t_j)}{\partial(x_i n_i)} - [\frac{3}{2\sqrt{2}} \frac{\partial(C)}{\partial(x_i)} n_i + \sigma \cos(\theta_e q) g\prime(C)] \frac{\partial(C)}{\partial(x_j)} t_j \tag{3.7}$$

$$\frac{\partial P}{\partial x_i} n_i = 0 \tag{3.8}$$

$$u_i n_i = 0 \tag{3.9}$$

In the following a numerical algorithm assuming a fully explicit approach is used .Actually in order to simplification, all the equations are solved explicitly.

3.2 Time integration and spatial discretisation

Here in this section, the staggered arrangement fundamental that used in this study along with discretization method are discussed.

3.3 Staggered arrangement

A full system of equations mentioned above, are solved on a Cartesian mesh with a staggered arrangement in which the velocity components are stored at the cell faces and the scalar variables such as pressure, chemical potential and the order parameter are defined at the cell centres. The main reason to use a staggered arrangement is to store the different variables is that coupling can be enforced, as uncoupling between pressure and velocities cause a number of problems. To be more specific, in order to solve the incompressible Navier-Stokes in the initial variables formulation, there is a need to discretise the pressure and the velocity components. Since, in the

staggered grid formation, pressure and velocity are stored in different locations (pressure at the cell centre and the velocity components at the centre of the cell faces) and this staggering of the variables, results in different control volumes for the velocity, momentum equations and the continuity equation; Hence, results in pressure-velocity coupling.

3.4 Spatial discretization

The second-order finite difference scheme is used for spatial discretisation in which the linear terms in the equations are discretized with usual second-order centered differences and the discretization of the nonlinear terms (convection terms) is obtained by a combination of second-order forward and backward differences.

3.5 Time integration

The different terms are advanced in time explicitly using the Adams-Bashforth scheme.

3.6 Fractional step

Eventually, The fractional-step method for incompressible two-fluid systems is implemented as in [21]. Fractional step (or projection) methods are a widely used technique for uncoupling the pressure solution in the incompressible Navier-Stokes equations while still satisfying the incompressibility constraint. This pressure-correction method that is used is a new method for simulating incompressible two-fluid flows with large density and viscosity ratios which is s 10–40 times faster than the standard pressure-correction method. This is due to that in this method a combination of fast Fourier transforms (FFT) and Gauss elimination is used in order to solve the Poisson equation directly in Fourier space.
First, an approximate velocity is computed by defining RU_i^n as

$$RU_i^n = -\frac{\partial(u_i^n u_i^n)}{\partial x_j} + \frac{1}{\rho^{n+1}}\frac{\partial}{\partial x_j}(\mu^{n+1}(\frac{\partial u_i^n}{\partial x_j} + \frac{\partial u_j^n}{\partial x_i})) + \frac{1}{\rho^{n+1}}\frac{\partial C^{n+1}}{\partial x_i} + F_b \tag{3.10}$$

which is the right-hand side of the momentum equation 3.1 without the pressure gradient term. The equations are integrated in time using the Adams-Bashforth scheme:

$$\frac{u_i^* - u_i^n}{\Delta t} = \frac{3}{2}RU_i^n - \frac{1}{2}RU_i^{n-1} \tag{3.11}$$

In the pressure-correction method, to satisfy the divergence-free condition (3.2), the velocity field is advanced in time by applying the pressure-correction to the approximate velocity, u^*, as

$$\frac{u_i^{n+1} - u_i^*}{\Delta t} = -\frac{1}{\rho^{n+1}}\frac{\partial p^{n+1}}{\partial x_i} \tag{3.12}$$

Then, by taking the divergence of Eq. 3.12 and imposing the divergence-free condition on u_i^{n+1}, we get a Poisson equation for pressure with a variable coefficient $(1/\rho^{n+1})$:

$$\frac{\partial}{\partial x_j}\left(\frac{1}{\rho^{n+1}}\frac{\partial p^{n+1}}{\partial x_j}\right) = \frac{1}{\Delta t}\frac{\partial u_j^*}{\partial x_j} \tag{3.13}$$

Eqs. (11),(12), and (13) are solved in a standard, two-fluid pressure-correction method, which we call the Unsplit method.
In our pressure-correction method, the goal is to obtain a constant Poisson equation in place of the variable coefficient Poisson equation (3.13). To this end, we split the pressure gradient term into a constant part $(1/\rho_0)$ and a variable part $(1/\rho^{n+1})$, and then treat the constant part implicitly and the variable part explicitly as

$$\frac{1}{\rho^{n+1}}\frac{\partial p^{n+1}}{\partial x_j} \longrightarrow \frac{1}{\rho_0}\frac{\partial p^{n+1}}{\partial x_j} + \left(\frac{1}{\rho^{n+1}} - \frac{1}{\rho_0}\right)\frac{\partial \hat{p}}{\partial x_j} \tag{3.14}$$

where $\rho_0 = min(\rho_1, \rho_2)$ for numerical stability and $\hat{p}$ which is an explicit approximation to the pressure at time level n+1 specifically,

$$\hat{p} = \begin{cases} p^n, & \text{if } J = 1 \\ p^* = 2p^n - p^{n-1}, & \text{if} J = 2 \end{cases} \tag{3.15}$$

The choice of $J = 1$ reduces the physical accuracy of the solution for flows with finite surface tension, therefore the choice $J = 2$ is required to accurately simulate flows with finite surface tension. Substituting (3.14) in Eq. (3.12) gives:

$$\frac{u_i^{n+1} - u_i^*}{\Delta t} = -\Big[\frac{1}{\rho_0}\frac{\partial p^{n+1}}{\partial x_i} + \left(\frac{1}{\rho^{n+1}} - \frac{1}{\rho_0}\right)\frac{\partial \hat{p}}{\partial x_i}\Big] \tag{3.16}$$

Then, by taking the divergence of (3.16) while imposing $\partial u_i^{n+1}/\partial x_i = 0$ yields a constant coefficient Poisson equation,

$$\frac{\partial^2 p^{n+1}}{\partial x_i^2} = \frac{\partial}{\partial x_i}\Big[\left(1 - \frac{\rho_0}{\rho^{n+1}}\right)\frac{\partial \hat{p}}{\partial x_i}\Big] + \frac{\rho_0}{\Delta t}\frac{\partial u_i^*}{\partial x_i} \tag{3.17}$$

which can be solved directly usin a fast Poisson solver. Finally, using (3.16), we update the velocity field by applying pressure-correction to u_i^* as

$$u_i^{n+1} = u_i^* - \Delta t\Big[\frac{1}{\rho_0}\frac{\partial p^{n+1}}{\partial x_i} + \left(\frac{1}{\rho^{n+1}} - \frac{1}{\rho_0}\right)\frac{\partial \hat{p}}{\partial x_i}\Big] \tag{3.18}$$

4

Results

The project consists of four different main test cases. Firstly, the results are presented from the canonical test cases of a droplet spreading over a horizontal flat walls with different surface wettabilities. Afterwards, four test cases for a droplet are performed on an inclined surface where the contact line dynamics depends on the inclination angle and surface wettability; eventually two test cases for a droplet are performed on an inclined surface with different wettabilities and also the wind velocity opposing the droplet spreading modelling the vehicle's windshield.

It is notable that for all of these test cases, not only the spreading radius is reported, but also the center of mass of the droplet is stated in order to have better comparison between different inclination and velocities.

Here, the initial frame and outline are observable as follows:

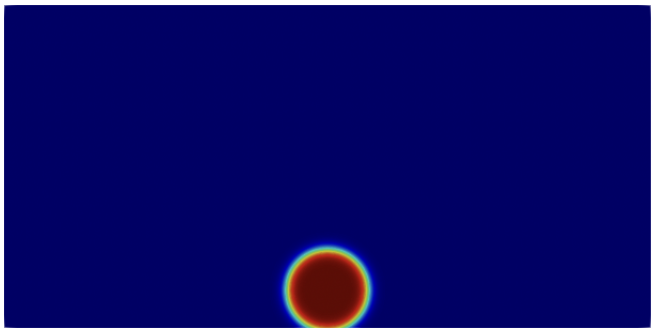

Figure 4.1: Initial Frame

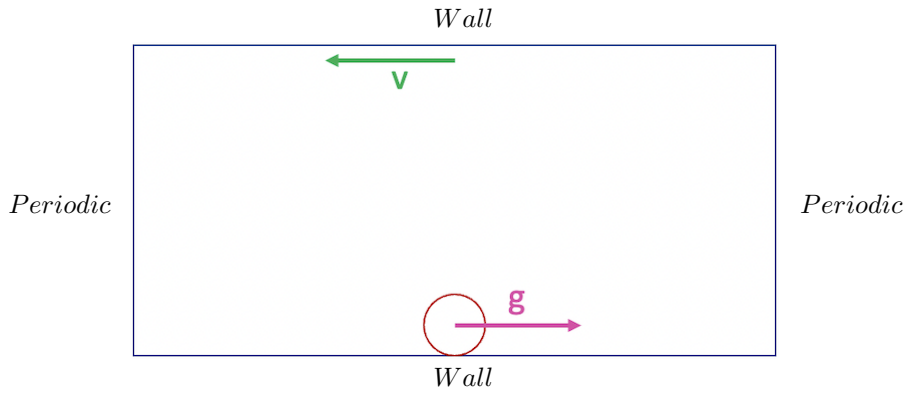

Figure 4.2: Outline

The Reynolds number(Re), Cahn(Cn), and Capillary numbers(Ca) are defined with a relation of initial droplet radius (R), the droplet's reference velocity($U_r = \frac{\sigma}{\mu}$), the surface tension coefficient (σ),interface thickness (ϵ) and the density of the liquid phase (ρ_l) .

$$Re = \frac{\rho U_r R}{\mu} \tag{4.1}$$

$$Cn = \frac{\epsilon}{R} \tag{4.2}$$

$$Ca = \frac{\mu U_r}{\sigma} \tag{4.3}$$

The Chan number must be defined as small as it is possible and also should be smaller than one due to the formulations. it is also dependent on grid sizes. It is mentionable as well that the the non-dimensional time which is used in order to compare different frames, is produced as follows.

$$t^* = \frac{t}{\sqrt{\frac{\rho R^3}{\sigma}}} \tag{4.4}$$

4.1 Droplet spreading on a flat surface

In this section, in order to discuss the results ,a two-dimensional circular droplet assumed that initially is placed on a flat surface (with two different wettabilities) so that the interface is almost tangent to the surface.

4.1.1 Test case 1

- $\theta = 45°$(Droplet spreading over hydrophilic surface)

For a droplet on a surface without inclination in a flat wall setup, spreading radius is studied for both hydrophilic($\theta = 45°$) and hydrophobic ($\theta = 135°$contact angle. It is notable that for some selected cases, slip velocity assumed in order to improve contact line singularity as it mentioned before.

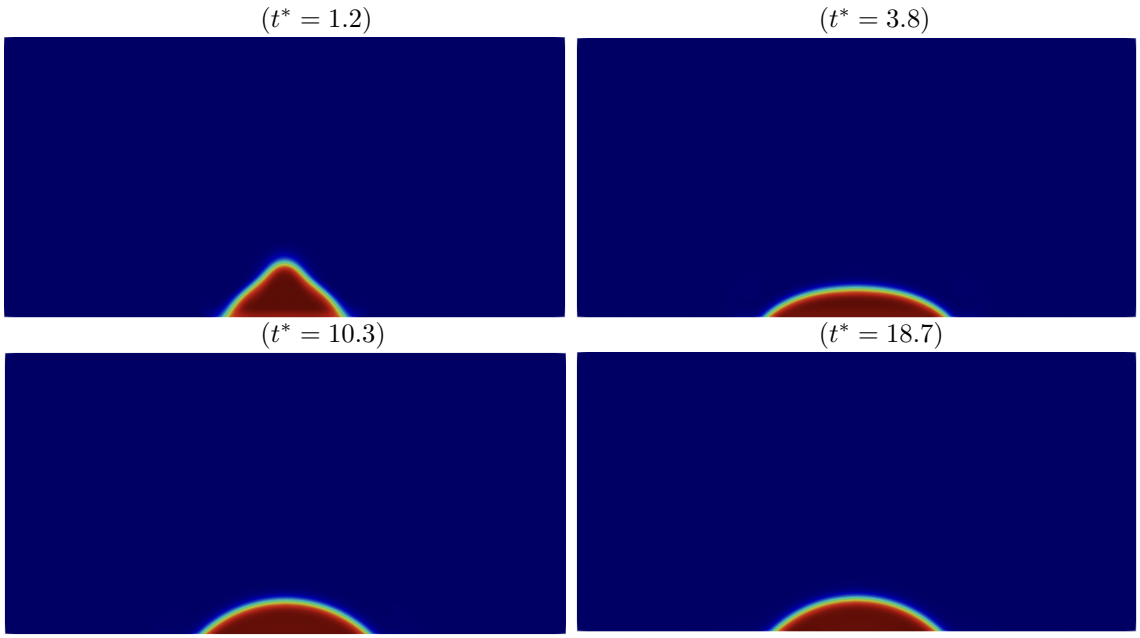

Figure 4.3: Variation in the spreading radius versus non-dimentionalized time on a hydrophilic flat surface

As it is observable from Figure 4.3 which shows the variation in spreading radius versus the non-denationalized time; the characteristics associated with the change in the spreading radius are the forward and backward pinning, which it is illustrates arise with time up to a point, hence it bounces till reaches a equilibrium. For the flat surface with hydrophilic wettability ($\theta = 45°$),the contact line of the growing droplet begins to move outward and the spreading radius grows significantly compared to the initial frame and increases. This is because higher surface tension (σ_{sl}) and interaction between this solid surface and the droplet than the hydrophobic surface.

4.1.2 Test case 2

- $\theta = 135°$(Droplet spreading over hydrophobic surface)

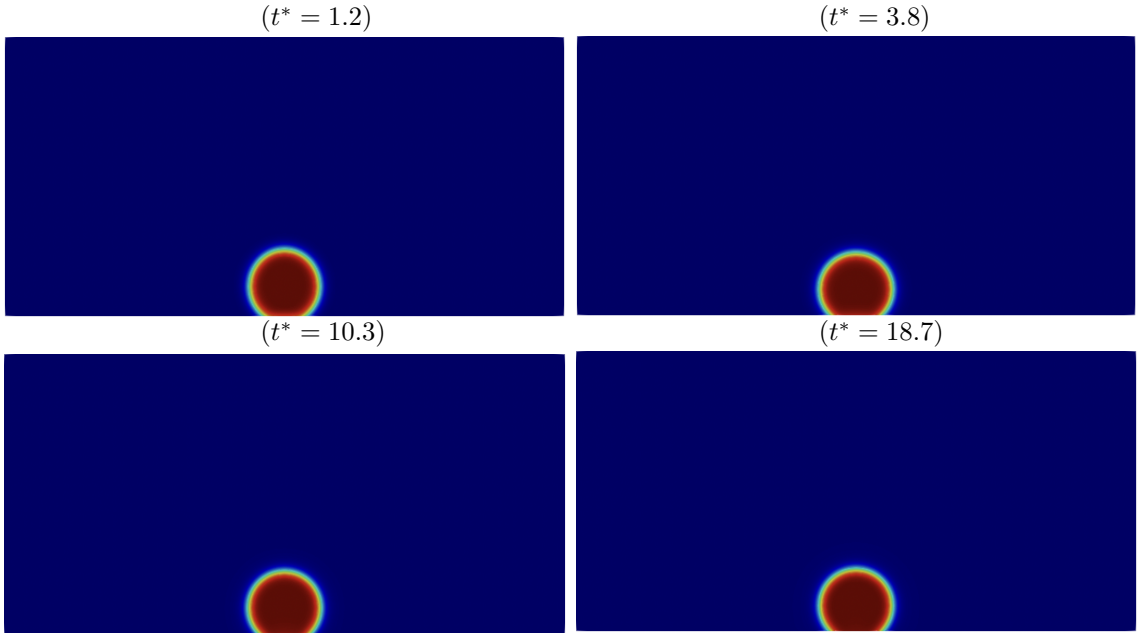

Figure 4.4: Variation in the spreading radius versus non-dimentionalized time on a hydrophobic flat surface

Hydrophobic surfaces have the property of repelling water as discussed in previous chapter.They do not easily become wetted in contact with water. The phenomenon is due to the unbalanced molecular forces at the water/solids interface which results in increasing surface tension, hence, more spherical shape after a while.

As it is observable from Figure 4.3, changing in the spreading radius versus time is very small compared to the previous test case in same time with different surface wettability.

When the solid has a high affinity for water in which case it is called hydrophilic (higher energy like glass) water spreads more. In the opposite case of hydrophobic (lower energy) surfaces, water does not spread but, instead, forms at equilibrium a spherical cap resting on the substrate with a contact angle.

4.1.3 Comparison of two different "Flat surface" test cases' Spreading radius

Here in this section, evolution of the normalized wetting radius (r/R) versus the non-dimensional time is observable. It is indicated that the hydrophilic case has higher wetting radius which is reasonable since the interfacial tension between the solid and liquid is higher because the interaction between the two is stronger. Hence, the droplet lose its shape faster.

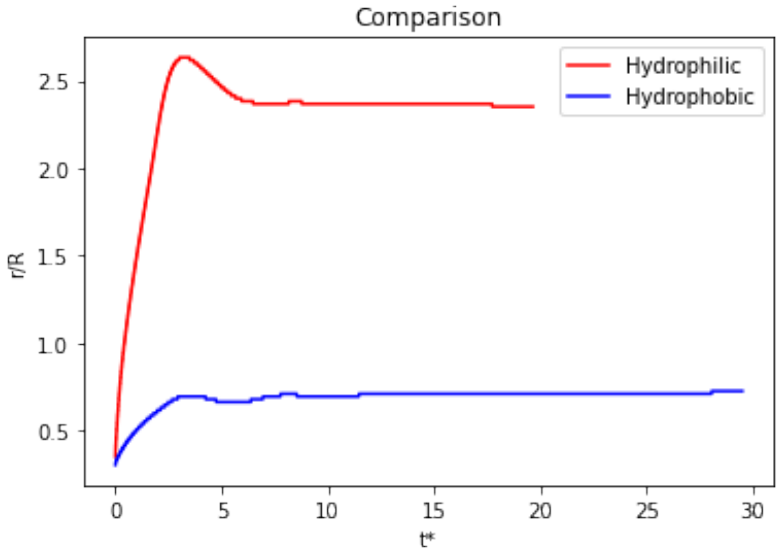

Figure 4.5: Figure 4.5 shows the evolution of the normalised wetting radius versus the non-dimensional time ($t^* = t/(\rho R^3/\sigma)^{(1/2)}$) for two different contact angles ($\theta_{eq} = 45°$ and $135°$) on a flat surface

4.1.4 Additional test cases with different Reynolds and Capillary numbers

In this section, capillary number has changed in order to have a better comparison between different test cases. In general, there are three forces governing the sprading dynamics which are inertial, viscous, and surface tension forces. By defining Reynolds and Capillary number, the dominant force changes.

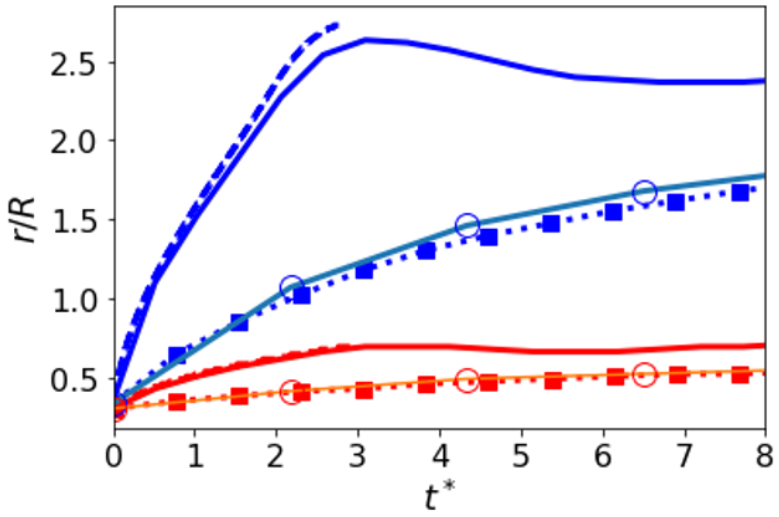

Figure 4.6: Figure 4.6 shows the evolution of the normalised wetting radius versus the non-dimensional time ($t^* = t/(\rho R^3/\sigma)^{(1/2)}$) for all different test cases on a flat surface

By looking at Figure 4.6, the firts outcome is that droplet spreads more on a hydrophilic surface due to stronger interfacial forces so, results in less vision for drivers. Moreover, in our study, viscous and the surface tension forces are of the same order (Ca=0.5 or 1), whereas inertial forces are three or one order of magnitude larger than the other two (Re=1000 or 10). For the higher Reynolds numbers, the lower the viscous forces are, hence, faster droplet spreading. At fixed Reynolds number and by decreasing the Capillary, the surface tension forces overcome the viscous ones; thus faster spreading is observable. Also it is mentionable that for the hydrophobic cases, the effects of Ca on the spreading is negligible when comparing to inertia (Re).

4.2 Droplet spreading on an inclined surface with different rotation angle

This test case includes a better representative of wetting phenomenon in automotive industry. Here in this test case, the spreading radius is reported for a droplet on an inclined surface (for two rotation angle $\alpha = 30°$ and $\alpha = 60°$) in an inclined surface setup for both hydrophilic($\theta = 45°$) and hydrophobic ($\theta = 135°$contact angle. Furthermore, for some selective cases, capillary number will be changed in order to have better comparison between different test cases.

4.2.1 Test case 1($\alpha = 30°$)

- $\theta = 45°$(Hydrophilic)

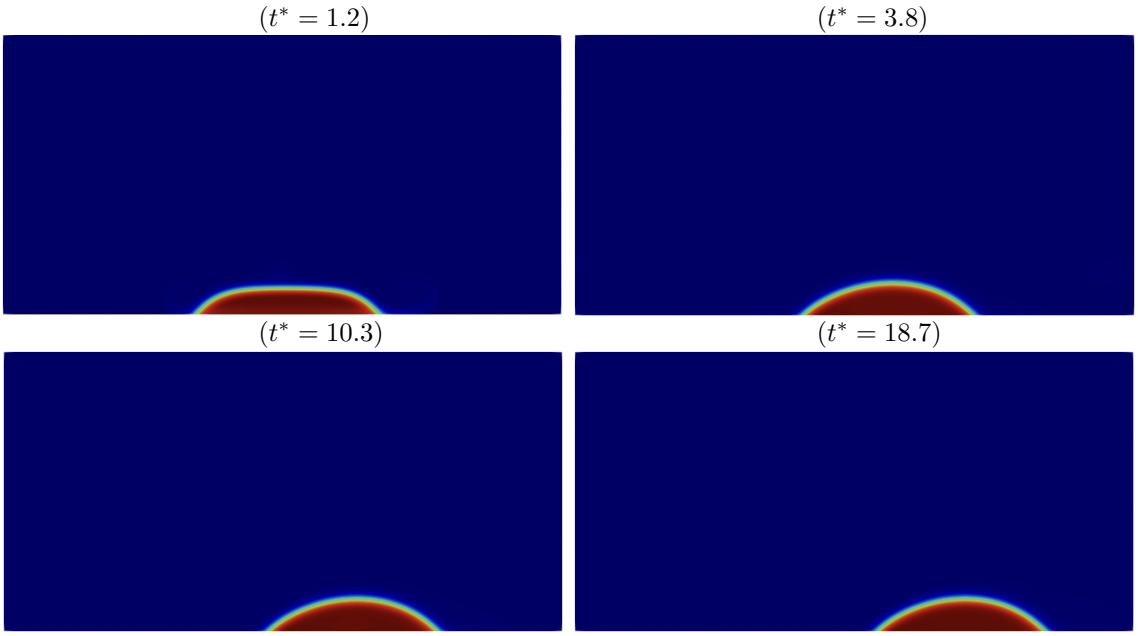

Figure 4.7: Variation in spreading radius versus non-dimentionalized time on hydrophilic Inclined surface with the rotation angle of ($\theta = 30°$)

- $\theta = 135°$(Hydrophobic)

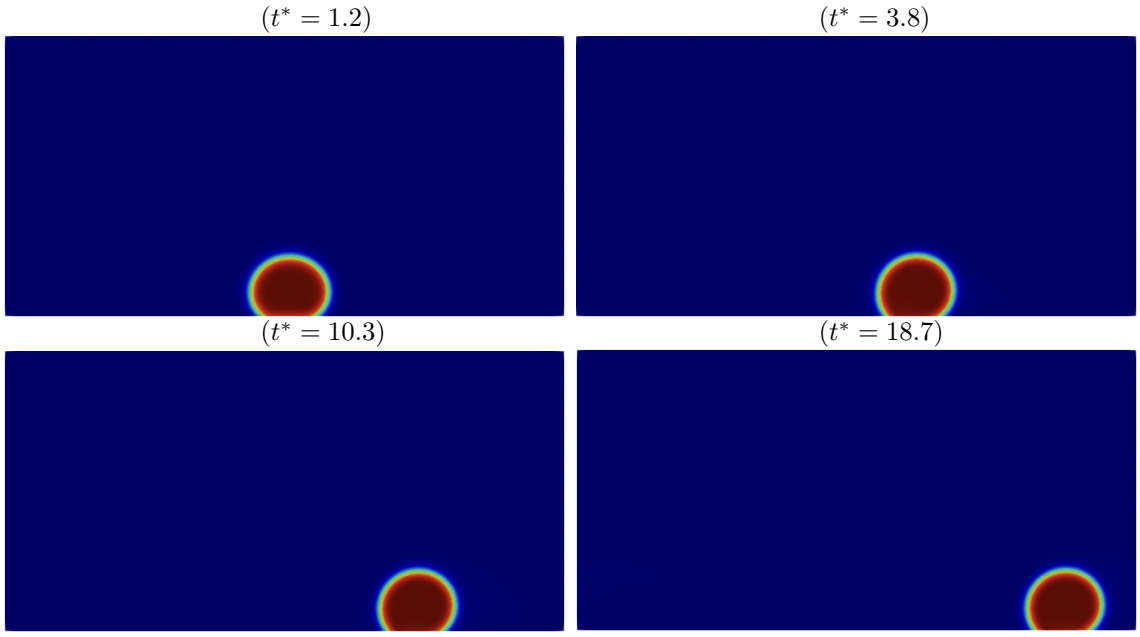

Figure 4.8: Variation in the spreading radius versus non-dimentionalized time on a hydrophobic Inclined surface with the rotation angle of ($\theta = 30°$)

As discussed in previous chapters, when a droplet is placed on a surface, it will spread on the surface based on the intermolecular interactions between the solid surface and the liquid. Water contact angle will immediately give an indication of the wettability of the solid surface. When the measured contact angle is above 90 degrees, the solid is said to have poor wetting and is termed hydrophobic and for the contact angle below than 90 degrees, a term hydrophilic is used. Moreover, it is observable form this section Figures 4.8 and 4.7 that with a rotation angle of the solid surface,the gravity acts downward along the positive y-axis, and since we are dealing with drops on an inclined surface, the droplet moves towards end of the domain due to the direction of the gravity.

4.2.2 Test case 2($\alpha = 60°$)

- $\theta = 45°$(Hydrophilic)

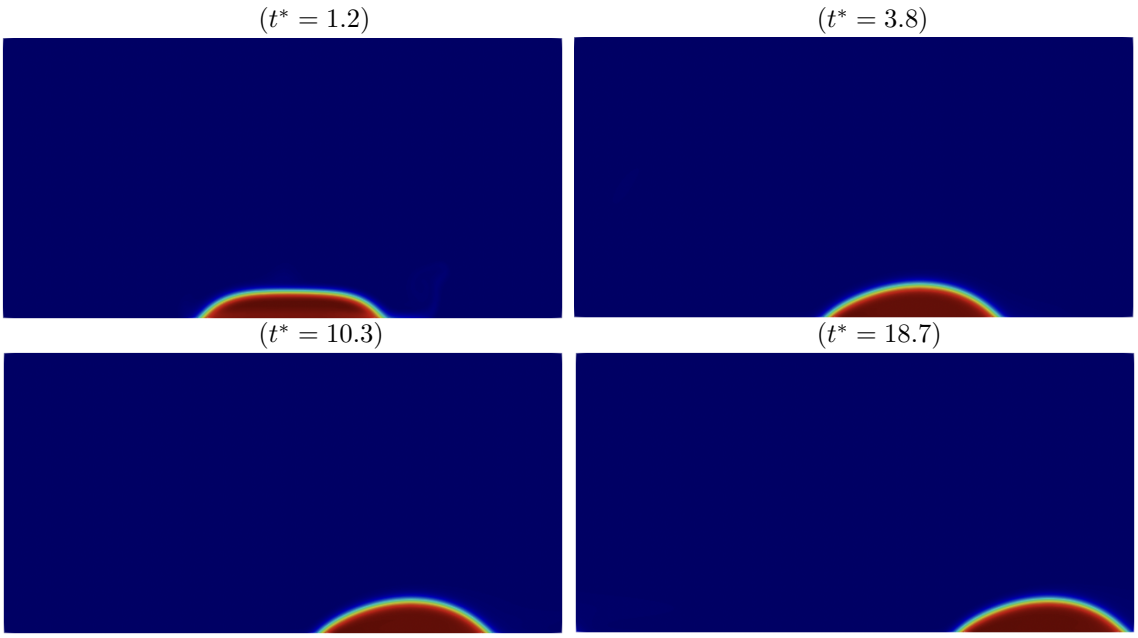

Figure 4.9: Variation in the spreading radius versus non-dimentionalized time on a hydrophilic Inclined surface with the rotation angle of ($\theta = 60°$)

- $\theta = 135°$(Hydrophobic)

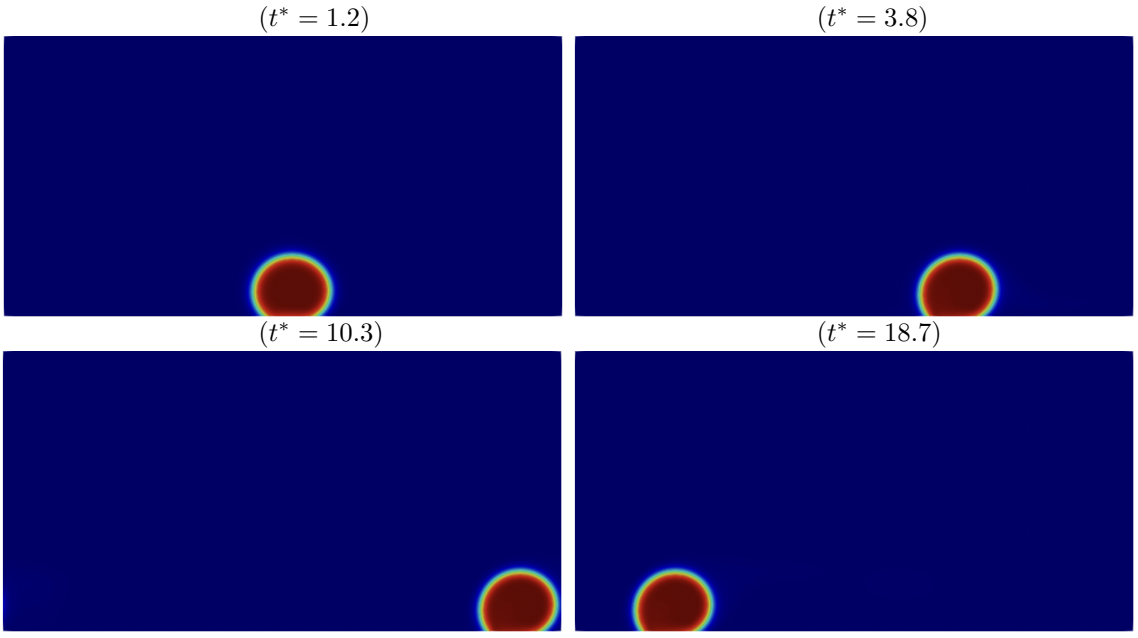

Figure 4.10: Variation in the spreading radius versus non-dimentionalized time on a hydrophobic Inclined surface with the rotation angle of ($\theta = 60°$)

It is observable from Figure 4.9 and 4.10that compared to previous test case with rotation angle of($\alpha = 30°$), higher rotation angle($\alpha = 60°$), results in faster movement of the droplet towards the end of the domain for both hydrophilic and hydrophobic surfaces. Hence, in automotive industry, the angle of windshield has a huge influence on faster rain drop movement towards down and therefore, faster cleaning and better vision for drivers.

As it is illustrated from Figure 4.10, not only higher contact but also the wettability of the surface has a great influence on faster movement of the droplets towards the end of the domain. It is indicated with both higher rotation angle and hydrophobic solid surface, it will end up in fastest movement of the droplet at same time. It is observable from the last frame of this figure that at a same time, the droplet is located near to the start of the domain. This is due to periodic boundary condition implemented for the simulations.In other words, with a Periodic domain, whatever flows into one side of the domain, is the same as on the other side;hence, with one period of simulation, the droplet next location would be at the start of the domain.

Therefore, in automotive industry making cars windshield as hydrophobic (water-repellent) as possible isn't just a smart design choice, it is also could be an investment in the safety. Indeed, hydrophobic coatings which are popular these days, are types of coatings that are applied to the automobile glass in order to give it self-cleaning properties. These coatings contain titanium oxide that causes water, dust and other small particles to be readily dispersed from windshield.

Moreover, it is notable that higher spreading radius for hydrophilic surfaces which is observable in Figure 4.11 is due to higher surface tension (σ_{sl}) and interaction between the solid surface and the droplet than the hydrophobic surface.

4.2.3 Comparison of four different test cases' Spreading radius and Center of mass

It is observable from Figure 4.11 that the wettability has the main influence on spreading radius. As it is illustrated, red and blue lines represents the results of the present simulations with $\theta = 45°$, and green and yellow lines indicates results for $\theta = 135°$. As it is shown in this figure, for larger inclination, there is slightly increases the inertial forces which resulting in faster motion and spreading of the droplet. But it is obvious that the influence of surface wettability is much higher.

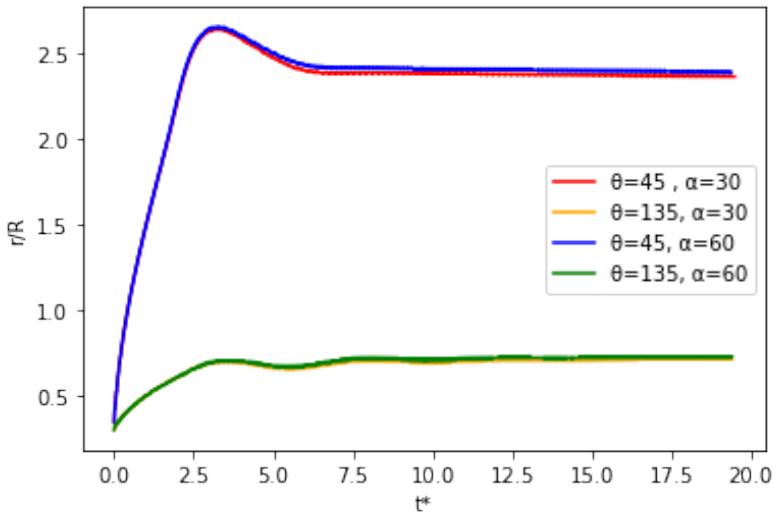

Figure 4.11: Figure 4.11 shows the evolution of the normalised wetting radius versus the non-dimensional time ($t^* = t/(\rho R^3/\sigma)^{(1/2)}$) for two different contact angles ($\theta_{eq} = 45°$ and $135°$) on an inclined surface

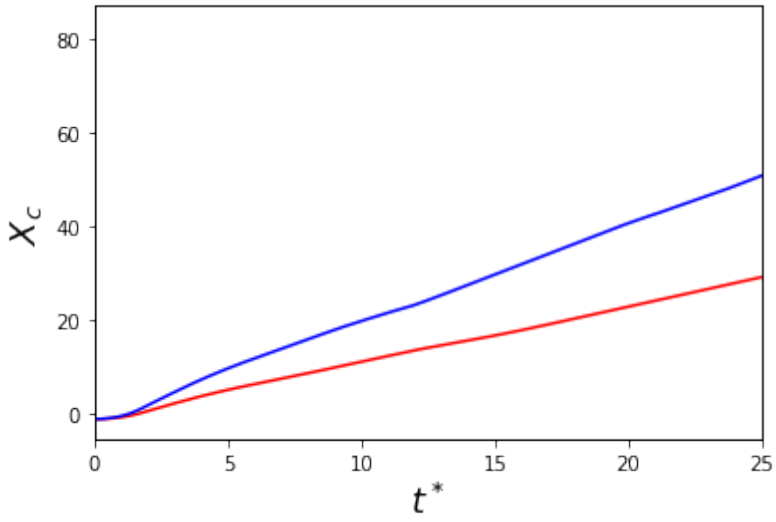

Figure 4.12: Figure 4.12 shows X center of mass values versus non-dimentionalized time($t^* = t/(\rho R^3/\sigma)^{(1/2)}$) for hydrophilic surfaces for two different Inclination angles ($\alpha_{eq} = 30°$ and C60°)

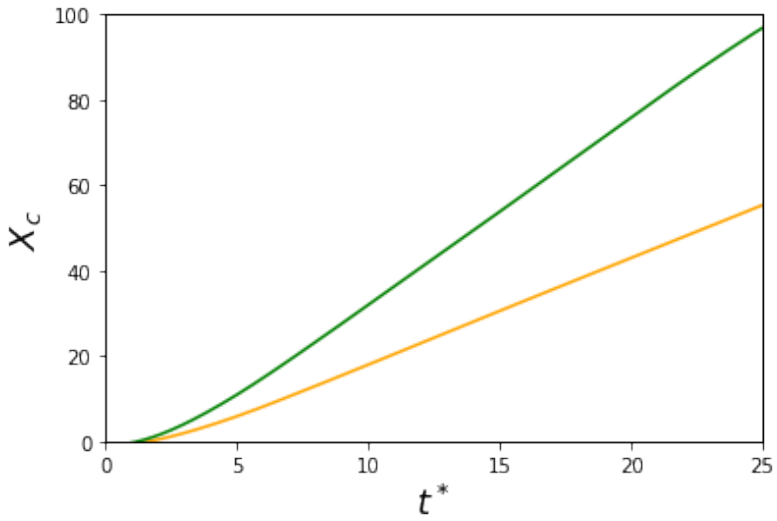

Figure 4.13: Figure 4.13 shows X center of mass values versus non-dimentionalized time($t^* = t/(\rho R^3/\sigma)^{(1/2)}$) for hydrophobic surfaces for two different Inclination angles ($\alpha_{eq} = 30°$ and $60°$)

Data on X_c suggests that, the same droplet travels about twice the distance on the hydrophobic wall. With comparing the results, up to t = 25 (for a constant α)it is observable that for hydrophobic sliding is about two times faster than hydrophilic.

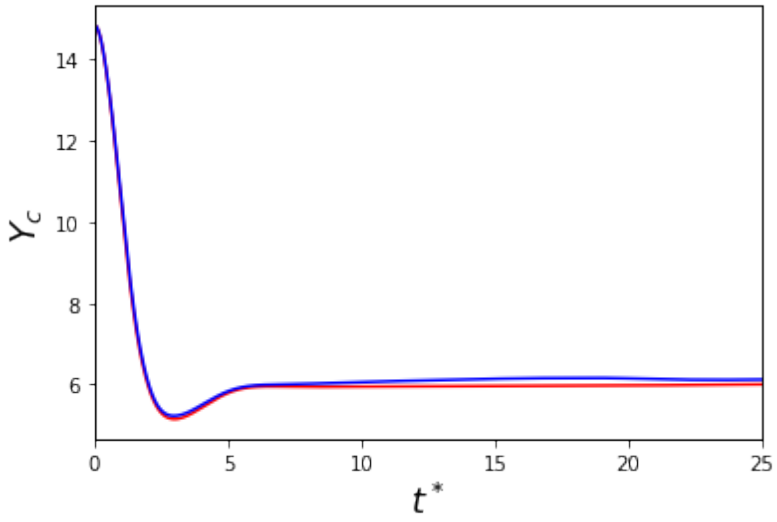

Figure 4.14: Figure 4.14 shows Y center of mass values versus non-dimentionalized time($t^* = t/(\rho R^3/\sigma)^{(1/2)}$) for hydrophilic surfaces for two different Inclination angles ($\alpha_{eq} = 30°$ and $60°$)

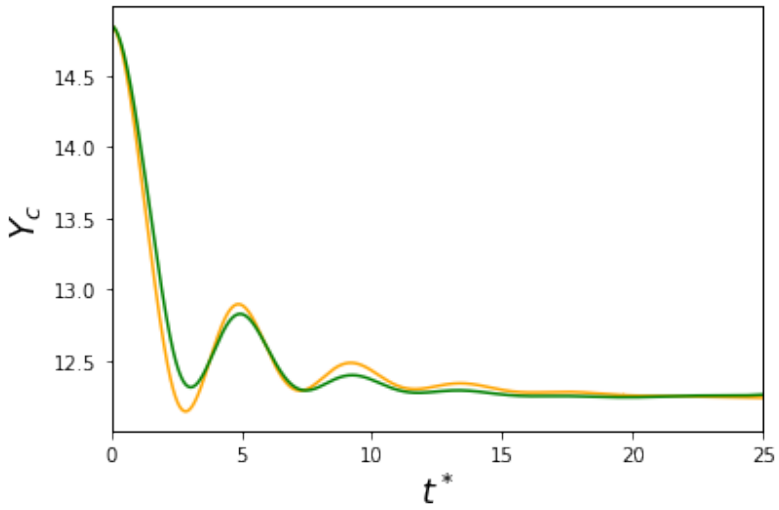

Figure 4.15: Figure 4.15 shows Y center of mass values versus non-dimentionalized time($t^* = t/(\rho R^3/\sigma)^{(1/2)}$) for hydrophobic surfaces for two different Inclination angles ($\alpha_{eq} = 30°$ and $60°$)

It is observable from X_c data that, droplet undergoes more bounces over a hydrophobic wall. This is all due to the molecular interactions betwee solid surface and liquid.

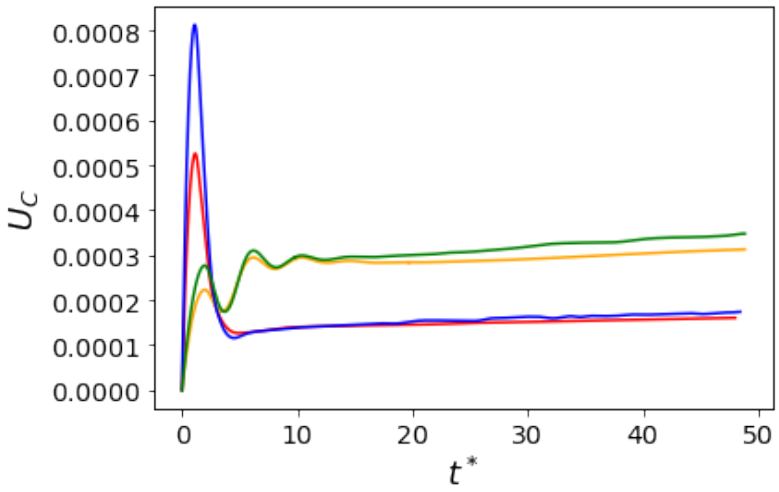

Figure 4.16: Figure 4.16 shows transposed center of mass velocity values versus non-dimentionalized time ($t^* = t/(\rho R^3/\sigma)^{(1/2)}$) for two different contact angles ($\theta_{eq} = 45°$ and $135°$) on two inclined surface with different rotation angles

The results from Figure 4.16 indicate that, in the beginnig, the droplet accelerates and sliding is dominant. Later, the dynamics is dictated by the surface tension which reduces the sliding velocity. Actually there would be a balance between spreading and sliding by passing time. Thus, the droplet spreads less and leaves the wall sooner over a hydrophobic wall which is suitable for windshields.

4.3 Droplet spreading on an inclined surface with different rotation angle against the wind

This test case which it completes previous test case, includes a perfect representative of wetting phenomenon on vehicles' windshield. Here in this test case, the spreading radius is reported for a droplet on an inclined surface (again for two rotation angle $\alpha = 30°$ and $\alpha = 60°$) in a setup against wind for both hydrophilic($\theta = 45°$) and hydrophobic ($\theta = 135°$) contact angle. This test case is much more better since this setup with a top wall velocity in the opposit direction could be a good representative of wind across the rain droplet on vehicle's windshield.

4.3.1 Test case 1($\alpha = 30°$)

- $\theta = 45°$(Hydrophilic)

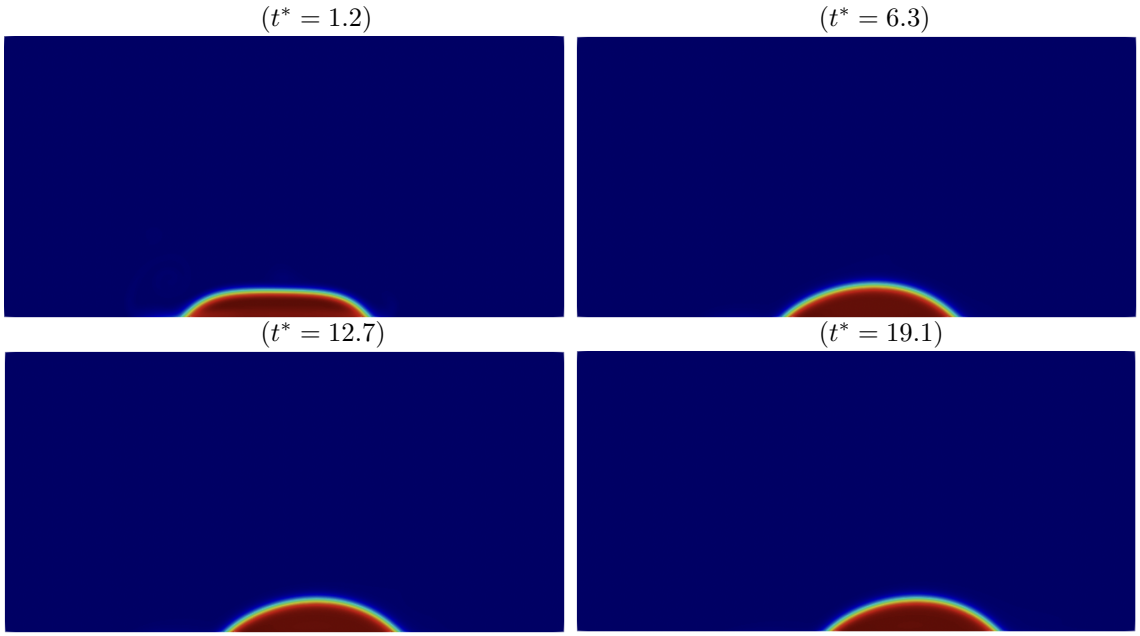

Figure 4.17: Variation in the spreading radius versus non-dimentionalized time on a hydrophilic Inclined surface with the rotation angle of ($\theta = 30°$) in a setup against the wind

It is indicated in Figure 4.17, compared to previous test case with same rotation angle ($\alpha = 30°$); in this test case there is a top wall velocity which could be a representative of wind in the opposite direction of a rain droplet moving on a windshield. It results in slower movement of the droplet towards the end of the domain.It is also observable from the first two figures of each test cases, that in the last frame of Figure 4.17 even with a later time; the droplet location in the set up against wind is further back compared to the one with an inclined wall setup. This is due to the top wall velocity which acts on the opposite direction of droplets movements and it is also a better representative of what exactly happens in industry.

* $\theta = 135°$(Hydrophobic)

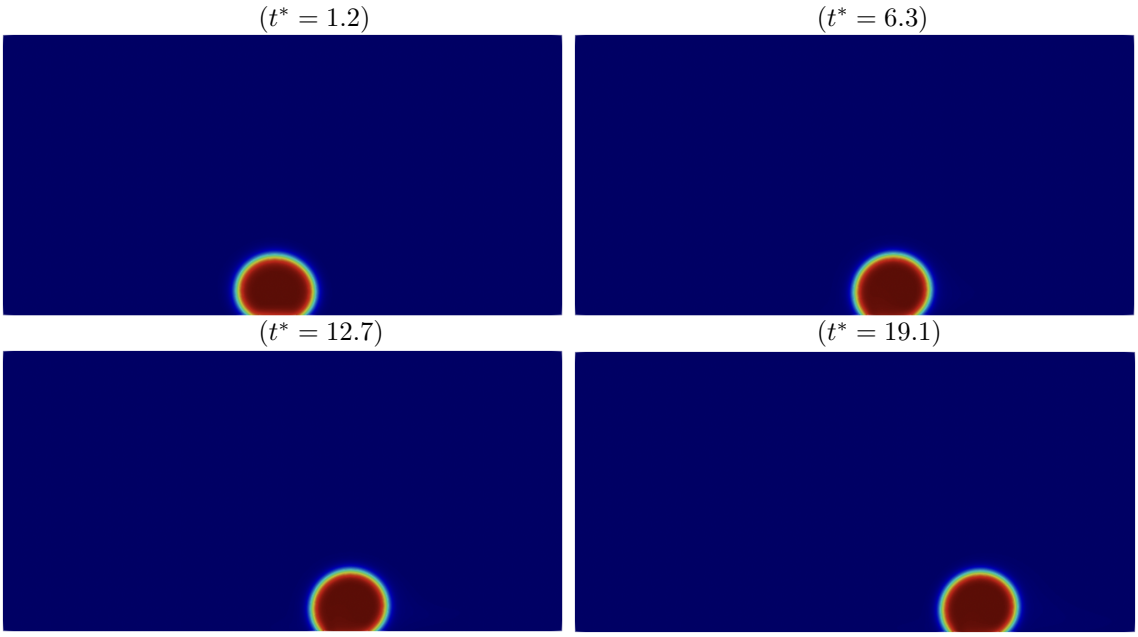

Figure 4.18: Variation in the spreading radius versus non-dimentionalized time on a hydrophobic surface with the rotation angle of ($\theta = 30°$) in a setup against the wind

Here in this test case it is indicated that since there is a top wall velocity acting on the opposite direction, the droplet movement is much more slower than in the case with inclined wall setup. Furthermore, as discussed before, form Figure 4.18 with a hydrophobic surface, it is observable that the hydrophobic case with its lower wetting radius due to its lower interfacial tension between the solid and liquid keeps its shape more intense compared to the droplet on the hydrophilic surface .

4.3.2 Test case 2($\alpha = 60°$)

- $\theta = 45°$(Hydrophilic)

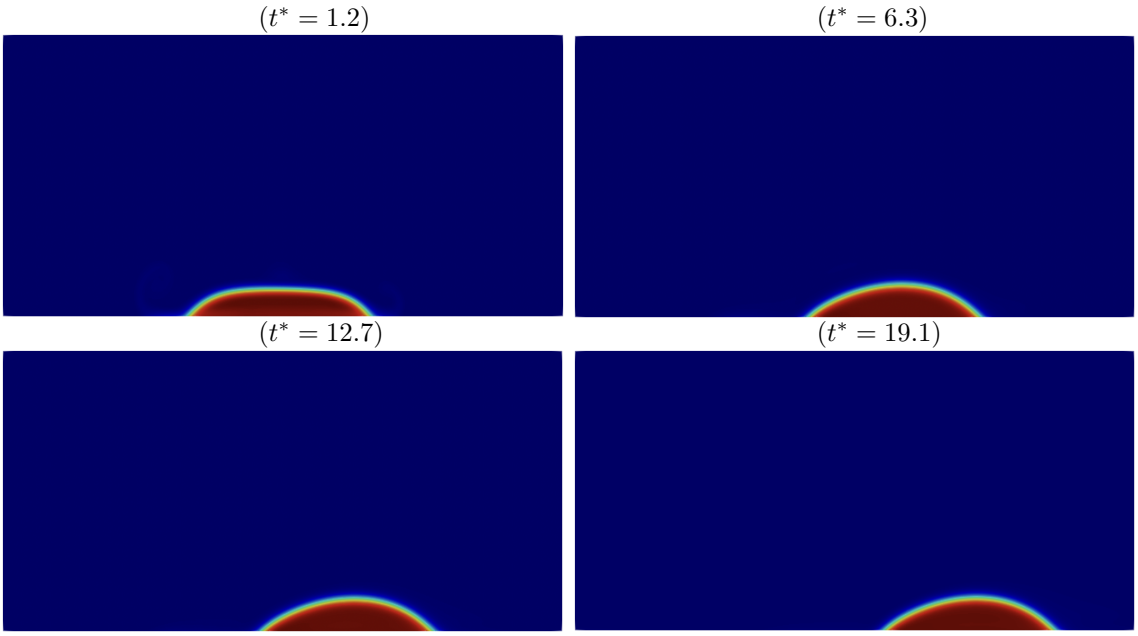

Figure 4.19: Variation in the spreading radius versus non-dimentionalized time on a hydrophilic surface with the rotation angle of ($\theta = 60°$) in a setup against the wind

- $\theta = 135°$(Hydrophobic)

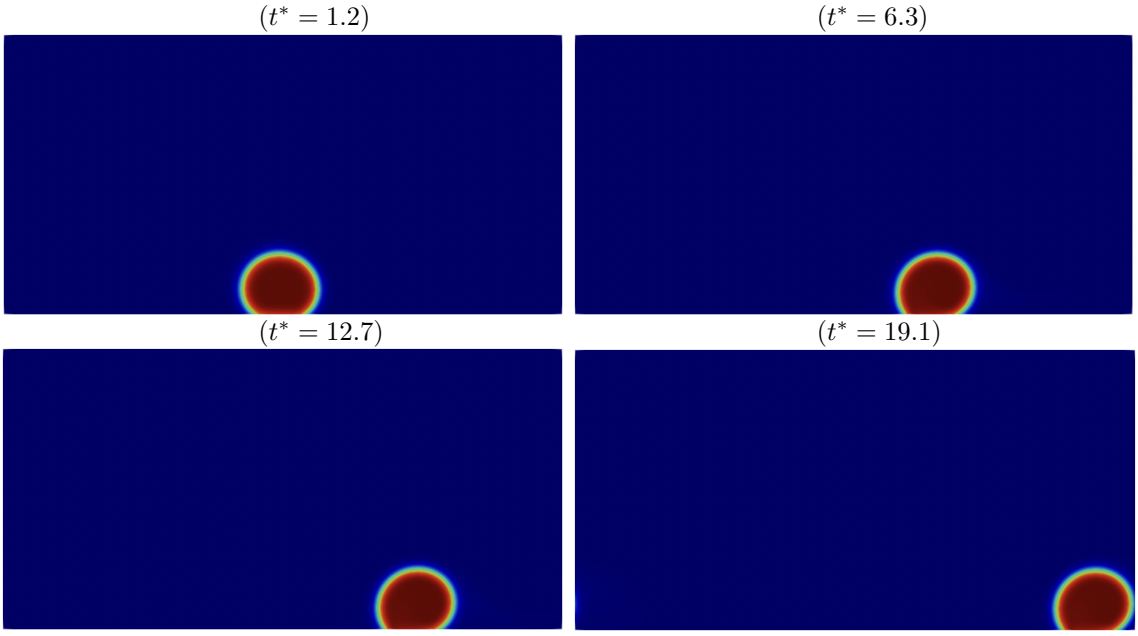

Figure 4.20: Variation in the spreading radius versus non-dimentionalized time on a hydrophobic surface with the rotation angle of ($\theta = 60°$) in a setup against the wind

4.3.3 Velocity profile of the test cases in an inclined setup against the wind

Figures in this section illustrate velocity profiles for all four different conditions in same non-dimentionalized time and frames.

By looking at velocity frames, for all of them it is observable that the high velocity region is much more concentrated in hydrophilic test cases. For hydrophilic test cases, there is a cocentrated high vlocity region towards back of the droplet by passing the time. This phenomenon results in having low pressure at the back of the droplet, hence; outcome is lower pressure difference and therefore pressure drag act on the droplet more than hydrophobic surface so; the droplet leaves the surface very soon on hydrophobic surface. Therefore, the hydrophobic surfaces are more suitable for windshields.

- $\theta = 45°$(Hydrophilic) and $\alpha = 30°$

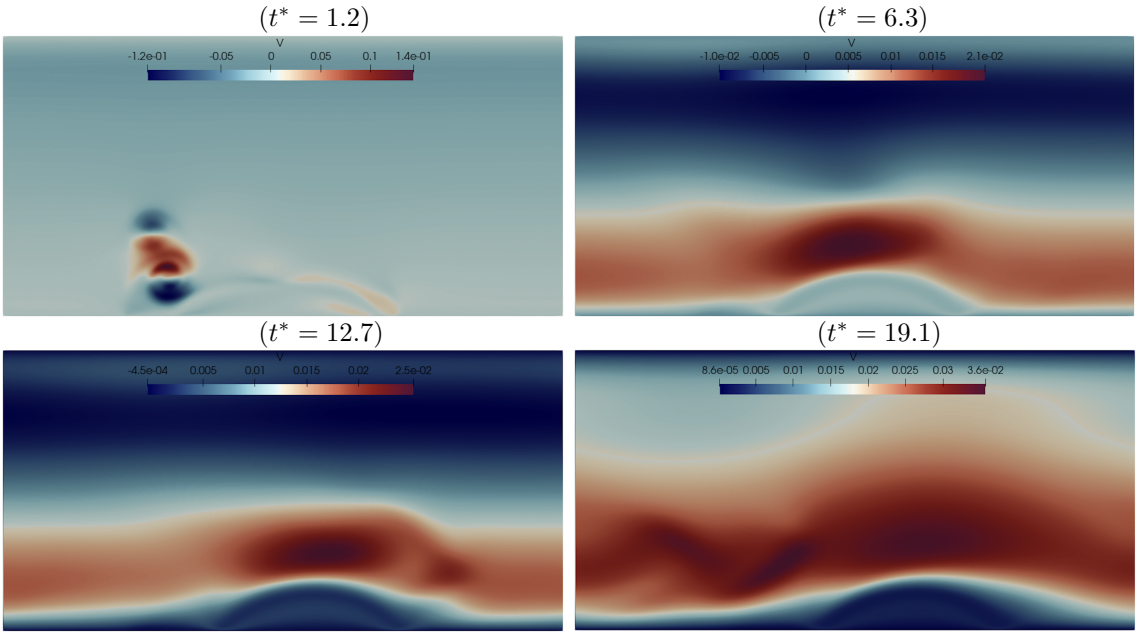

Figure 4.21: Variation in the velocity profile versus non-dimentionalized time on a hydrophilic surface with the rotation angle of ($\theta = 30°$) in a setup against the wind

- $\theta = 135°$(Hydrophobic) and $\alpha = 30°$

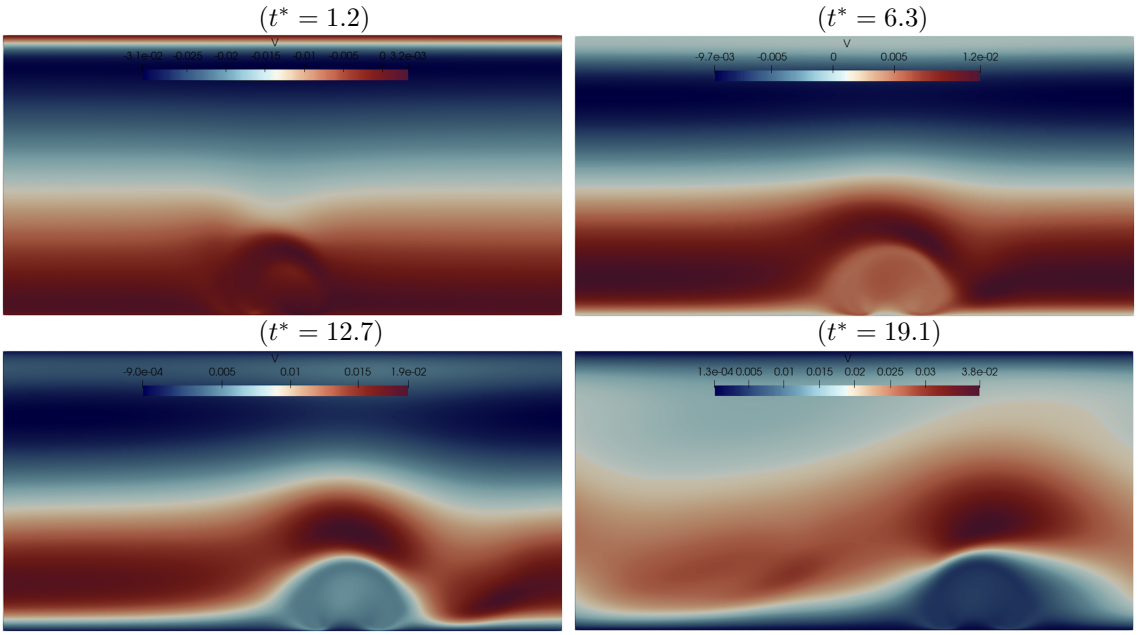

Figure 4.22: Variation in the velocity profile versus non-dimentionalized time on a hydrophobic surface with the rotation angle of ($\theta = 30°$) in a setup against the wind

mm

- $\theta = 45°$(Hydrophilic) and $\alpha = 60°$

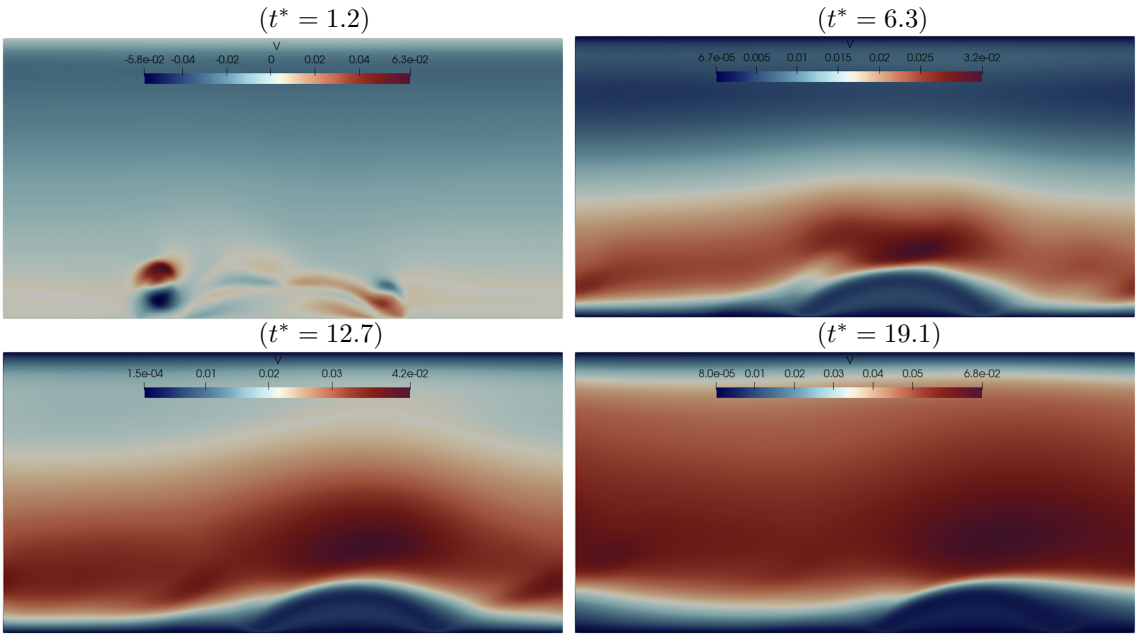

Figure 4.23: Variation in the velocity profile versus non-dimentionalized time on a hydrophilic surface with the rotation angle of ($\theta = 60°$) in a setup against the wind

- $\theta = 135°$(Hydrophobic) and $\alpha = 60°$

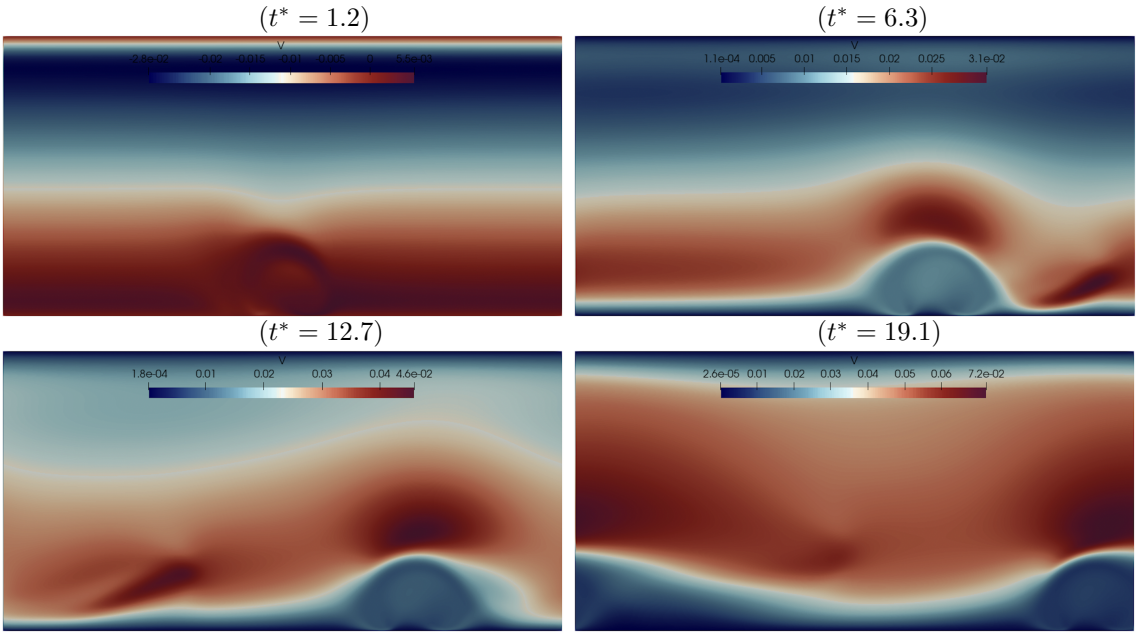

Figure 4.24: Variation in the velocity profile versus non-dimentionalized time on a hydrophobic surface with the rotation angle of ($\theta = 60°$) in a setup against the wind

4.3.4 Comparison of different test cases' Spreading radius and Center of mass in the inclined surface against the wind setup

For Figure 4.25 blue lines represent the results of the hydrophilic surface $\theta = 45°$and red lines show the results of the hydrophobic surface $\theta = 135°$. Moreover, the results with different Reynolds and Capillary numbers can be recognized by the lables for each Figure.

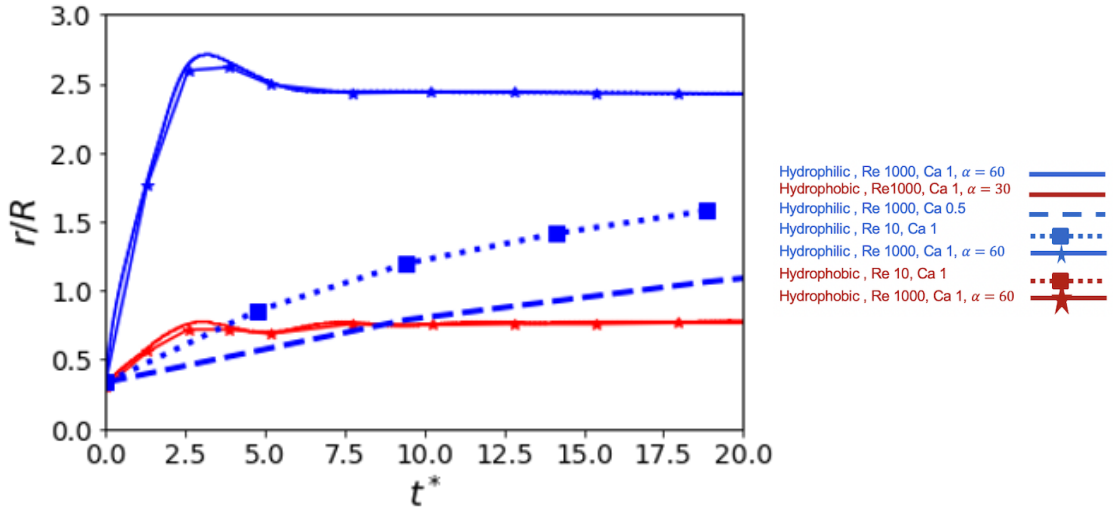

Figure 4.25: Figure 4.25 shows the evolution of the normalised wetting radius versus the non-dimensional time ($t^* = t/(\rho R^3/\sigma)^{(1/2)}$) for two different contact angles ($\theta_{eq} = 45°$ and $135°$) on an inclined surface

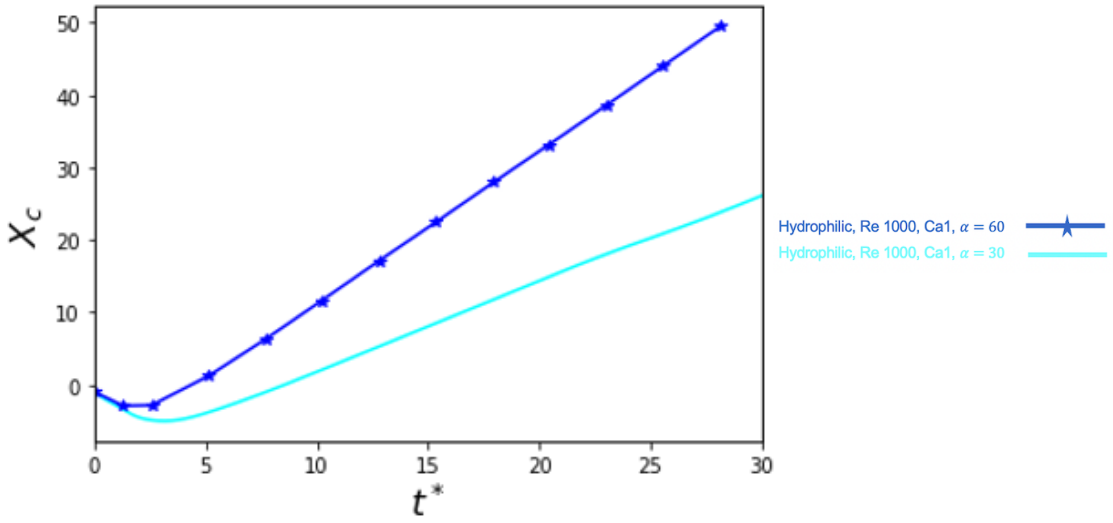

Figure 4.26: Figure 4.26 shows X center of mass values versus non-dimentionalized time($t^* = t/(\rho R^3/\sigma)^{(1/2)}$) for hydrophilic surfaces for two different inclination angles against the wind ($\alpha_{eq} = 30°$ and C60°)

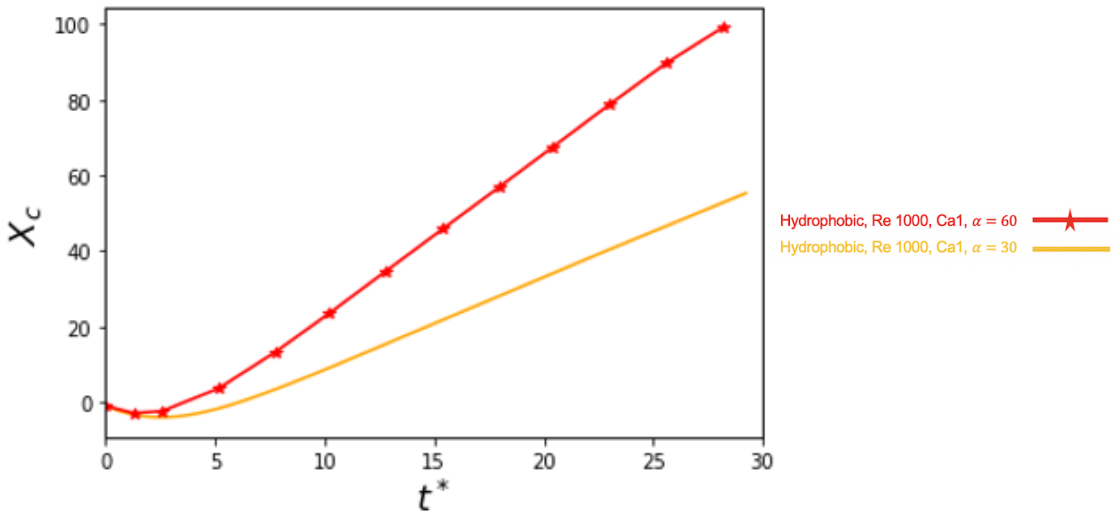

Figure 4.27: Figure 4.27 shows X center of mass values versus non-dimentionalized time($t^* = t/(\rho R^3/\sigma)^{(1/2)}$) for hydrophobic surfaces for two different inclination angles against the wind ($\alpha_{eq} = 30°$ and $60°$)

Again with this test cases' result, data on X_c suggests that, the same droplet travels about twice the distance on the hydrophobic wall. With comparing the results, up to t = 25 (for a constant α) it is observable that for hydrophobic sliding is about two times faster than hydrophilic.

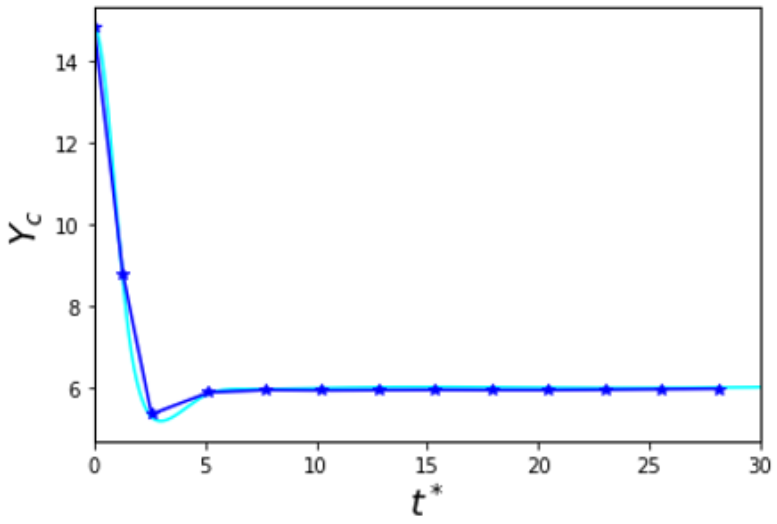

Figure 4.28: Figure 4.28 shows Y center of mass values versus non-dimentionalized time($t^* = t/(\rho R^3/\sigma)^{(1/2)}$) for hydrophilic surfaces for two different Inclination angles ($\alpha_{eq} = 30°$ and $60°$)

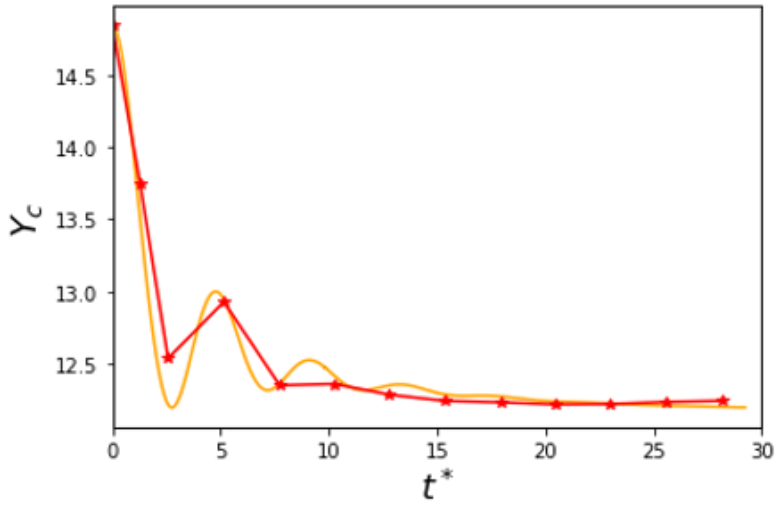

Figure 4.29: Figure 4.29 shows Y center of mass values versus non-dimentionalized time($t^* = t/(\rho R^3/\sigma)^{(1/2)}$) for hydrophobic surfaces for two different Inclination angles ($\alpha_{eq} = 30°$ and $60°$)

Similar observations as in the cases without any opposing wind are made for Re=1000 since the inertial forces are dominant and wind velocity is weak. It is observable from Y_c data that, droplet undergoes more bounces over a hydrophobic wall.

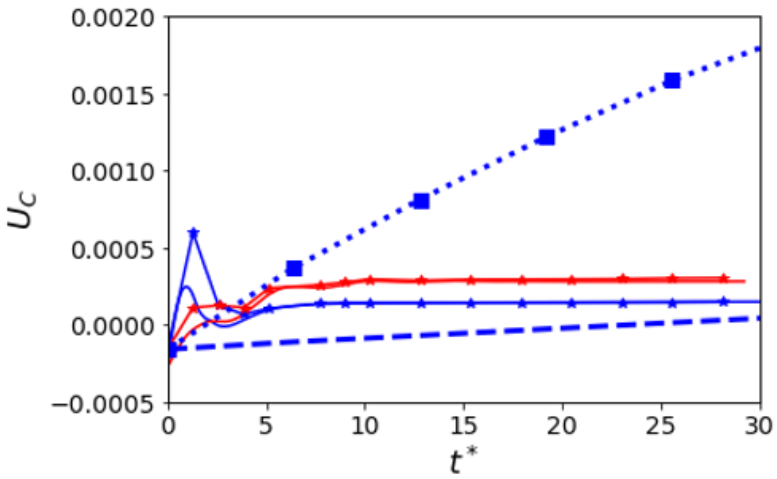

Figure 4.30: Figure 4.30 shows transposed center of mass velocity values versus non-dimentionalized time ($t^* = t/(\rho R^3/\sigma)^{(1/2)}$) for two different contact angles ($\theta_{eq} = 45°$ and $135°$) on two inclined surface with different rotation angles

The results from Figure 4.25 and Figure 4.30 indicate that, For lower Reynolds number(Re = 10) with constant Capillary (Ca = 1) the inertia of the system is lower, hence; surface tension and viscous forces become more important. Therefore, the droplet dynamics is governed by surface tension forces so there is spreading rather than sliding . Moreover, the velocity of the center of mass continuously increases

without any initial peak.Thus, the droplet spreads less and leaves the wall sooner over a hydrophobic wall which is suitable for windshields. At lower Reynolds number the droplet dynamics reaches the steady state much later than for large Reynolds number. The velocity of the center of mass continuously increases without any initial peak.Thus, the droplet spreads less and leaves the wall sooner over a hydrophobic wall which is suitable for windshields. The wettability of the surface has the main influence on spreading radius in general.

5

Discussion and Conclusion

This chapter discusses the results from the previous chapter and compares the outcomes as well. There are three different sections in which two sections discuss the comparisons between different test cases and their overall performance. The last part discusses some suggestions for further research and improvements.

5.1 comparison between different test cases

The project consists of three different main test cases in with different setups. For all test cases, the results has been investigated on both "Hydrophilic" and "Hydrophobic" surfaces.

It is observable from Figures 4.3, 4.4 and also 4.5, for the first test case on a horizontal flat surface, variation in spreading radius versus the non-denationalized time, for the flat surface with hydrophilic wettability ($\theta = 45°$),the contact line of the growing droplet begins to move outward and the spreading radius grows significantly compared to the initial frame . But for the surface with hydrophobic wettability ($\theta = 135°$) changing in the spreading radius versus time is very small and the droplet keeps its spherical shape more which make sense since the surface tension is higher due to unbalanced molecular forces at the water/solids interface. There are also some test cases with different Reynolds and Capillary number in order to have better comparison in different situations.

The results of second test case for a droplet on an inclined surface setup discuss the influence of different rotation angle on rolling off the droplet from surface. With comparing Figures 4.8 , 4.10 and 4.11 for hydrophobic surfaces, higher rotation angle has a great influence on faster movement of the droplet towards the end of the domain. Hence, with considering a good aerodynamic design, even a little higher rotation angle along with hydrophobic coating result in better self-cleaning of the windshield and therefore greater visibility and safety for the drivers.

The test instances for the third test case with similar condition but in a different setup indicates better representative of wetting phenomenon on vehicles' windshield. Moreover, in this setup for both hydrophilic($\theta = 45°$) and hydrophobic ($\theta = 135°$) contact angle, a top wall velocity in the opposite direction applied which is a good representative of wind across the rain droplet on vehicle's windshield.

It is observable from Figures 4.18, 4.20 and 4.25 the spreading radius follow same trend as previous test cases but the droplet movement is much more slower than in the case without wind due to an applied velocity in opposite direction of inclination. This is comparable from mentioned figures last frame in a same time. On the other hand, as discussed before, a hydrophobic surface with its lower wetting radius due to its lower interfacial tension between the solid and liquid keeps its shape more spherical compared to the results for a droplet on the hydrophilic surface.

5.2 Overall comparison

Comparing the results overall, there are three forces governing the sprading dynamics which are inertial, viscous, and surface tension forces. Due to the value of Reynolds and Capillary numbers, the domination of these forces change.

Droplet spreads more on a hydrophilic surface in all setups due to the stronger interfacial forces . In this study, viscous and the surface tension forces are of the same order (Ca =0.5 or 1), whereas inertial forces are three or one order of magnitude larger than the other two (Re =1000 or 10). Thus, for higher the Reynolds numbers, the lower the viscous forces, and the faster droplet spreading is observable. At fixed Reynolds number, by decreasing the Capillary number, the surface tension forces overcome the viscous ones; therefore again faster spreading is observable.
At smaller Reynolds number (Re = 10), the inertia of the system is lower, surface tension and viscous forces become more important for constant Capillary number (Ca=1).Thus, the droplet dynamics is governed by surface tension forces.Also, The droplet dynamics reaches the steady state much later than for large Reynolds number.
Eventually, by looking at center of mass location and velocity in different test cases, it is indicated that the droplet undergoes more bounces and travels twice the distance on the hydrophobic wall.

5.3 Further improvements

For further improvements, droplet impact and sliding over surfaces with different wettabilities can be examined in order to extend this current study. Moreover, the same Phase Field formulation and code can be used to study ice-formation on windshield. In order to have a more comprehensive study, coupling the same formulation with the heat transfer equation is approachable to study the effect of the temperature inside the car on the droplet spreading over the windshield. Moreover, simulations can be perform in 3 dimension as well.

Bibliography

[1] Carlson, A. et al, 2012. Jurnal of Phys. Rev. E. Universality in dynamic wetting dominated by contact-line friction . doi:10.1103/ PhysRevE.85.045302.

[2] Yada, S. , 2019. Wetting dynamics on asymmetric micro-structured surfaces 2019. https://doi.org/10.1039/C9SM01854A

[3] Cahn, J.W. , 1961. On spinodal decomposition. Acta Metallurgica 9, 795–801. URL: http://www.sciencedirect.com/science/article/pii/ 0001616061901821, doi:10.1016/0001-6160(61)90182-1.

[4] Moffatt, H. , 1964. Viscous and resistive eddies near a sharp corner. Journal of Fluid Mechanics, 18(1), 1-18. doi:10.1017/S0022112064000015

[5] Dussan, E.B., 1979. On the spreading of liquids on solid surfaces: Static and dynamic contact lines. Annual Review of Fluid Mechanics 11, 371–400.

[6] Sui, Y. et al, 2013. Numerical simulations of flows with moving contact lines. Annual Review of Fluid Mechanics 46, 97–119. doi:/10.1146/ annurev-fluid-010313-141338.

[7] Dervaux and Limat , 2015. Contact lines on soft solids with uniform surface tension https://doi.org/10.1098/rspa.2014.0813

[8] Yuri Y. T. , 2005. Simple analytical model of capillary flow in an evaporating sessile drop https://doi.org/10.1103/PhysRevE.71.027301

[9] Salem, T.K. et al , 2018 . "An experimental and analytical study on the influence of superhydrophobic micro-textured surfaces on liquid wetting phenomena." Colloids and Surfaces A: Physicochemical and Engineering Aspects

555 (2018): 191-200.

[10] Schäffer, E. , Wong, P. , 2000 .Contact line dynamics near the pinning threshold: A capillary rise and fall experiment.https://doi.org/10.1103/PhysRevE.61.5257

[11] Wilson, M. et al , 2006. Nonlocal hydrodynamic influence on the dynamic contact angle: Slip models versus experiment. DOI:https://doi.org/10.1103/PhysRevE.73.041606

[12] Boinovich and Emelyanenko , 2012. A wetting experiment as a tool to study the physicochemical processes accompanying the contact of hydrophobic and superhydrophobic materials with aqueous media https://doi.org/10.1016/j.cis.2012.06.010

[13] Wang, J. et al , 2009. Investigation on hydrophobicity of lotus leaf: Experiment and theory https://doi.org/10.1016/j.plantsci.2009.02.013

[14] Peskin, C.S. , 2002. The immersed boundary method. Acta Numerica 11, 479–517. doi:10.1017/S0962492902000077.

[15] Shahmardi, A. et al , 2021. A fully Eulerian hybrid immersed boundary-phase field model for contact line dynamics on complex geometries https://www.researchgate.net/publication/351899355

[16] Renardy, M. et al , 2001. Numerical Simulation of Moving Contact Line Problems Using a Volume-of-Fluid Method https://doi.org/10.1006/jcph.2001.6785

[17] Spelt, P. , 2014. Numerical Simulations of Flows with Moving Contact Lines https://doi.org/10.1146/annurev-fluid-010313-141338

[18] Young, T. , 1805. An essay on the cohesion of fluids. Royal Society 95. doi:doi.org/10.1098/rstl.1805.0005.

[19] Jacqmin, D. , 1999. Calculation of Two-Phase Navier–Stokes Flows Using Phase-Field Modeling. Journal of Computational Physics 155, 96–127. URL: http://www.sciencedirect.com/science/article/pii/ S0021999199963325, doi:10.1006/jcph.1999.6332.

[20] Jacqmin, D., 2000. Contact-line dynamics of a diffuse fluid interface. Journal of Fluid Mechanics 402, 57–88. doi:10.1017/S0022112099006874.

[21] Dodd, M.S., Ferrante, A., 2014. A fast pressure-correction method for incompressible two-fluid flows. Journal of Computational Physics 273, 416 – 434. URL: http://www.sciencedirect.com/science/article/pii/ S0021999114003702, doi:https://doi.org/10.1016/j.jcp.2014.05.024.

DEPARTMENT OF SOME SUBJECT OR TECHNOLOGY
CHALMERS UNIVERSITY OF TECHNOLOGY
Gothenburg, Sweden
www.chalmers.se

CHALMERS
UNIVERSITY OF TECHNOLOGY